Results in Engineering 32 (2026) 113995

Contents lists available at ScienceDirect

Results in Engineering

journal homepage: www.sciencedirect.com/journal/results-in-engineering

Review article

Interface-centred co-design of solid-state lithium batteries: An evidence-graded assessment of electrolytes, electrodes and ai-guided discovery

Mohammed Tihtih [a,*], Abdellah Ben yahia [b], Redouane En-nadir [c], M. A. Basyooni-M. Kabatas [d,e], István Kocserha [a]

[a] Institute of Energy, Ceramics, and Polymer Technology, University of Miskolc, H-3515, Egyetemvaros, Miskolc, Hungary
[b] Laboratory of Analytical Chemistry and Electrochemistry, Faculty of Sciences, Processes and Environment Team, URL-CNRST N 13, Moulay Ismail University, BP 11201, 50000, Zitoune, Meknes, Morocco
[c] 3IT, Faculty of Engineering, 2500 Bd de l'Université, Sherbrooke, QC, J1N 3C6, Canada
[d] Institute of Nanotechnology (INT), Karlsruhe Institute of Technology (KIT), Kaiserstra﷽e 12, 76131, Karlsruhe, Germany
[e] Department of Metallurgical and Materials Engineering, Faculty of Engineering, University of Dokuz Eylül, Izmir, Turkey

ARTICLE INFO

Keywords:
Solid-state battery
Solid electrolyte
Electrode–electrolyte interface
Interphase
Chemo-mechanics
Lithium-metal anode
Solid polymer electrolyte
Interface characterisation
Evidence grading
Machine learning
Machine-learning interatomic potentials
Data quality
Co-design

ABSTRACT

Solid electrolytes are widely expected to replace flammable liquid electrolytes in lithium batteries, yet cell-level progress has lagged behind the large gains in bulk ionic conductivity achieved over the past decade. This review argues that the electrode–electrolyte interface, rather than the bulk electrolyte, should be the unit of design, and examines the consequences of this view for engineering practice and for artificial intelligence (AI)-guided discovery. Using a documented, non-systematic literature selection (mainly 2018–2026, with earlier foundational work), we first re-examine the safety premise: removing the liquid removes one fuel, but thermal-runaway pathways remain through cathode oxygen release, lithium-metal reactivity, and stored electrical energy. We then compare oxide, sulfide, halide/oxyhalide, solid polymer, gel/quasi-solid, and composite electrolytes, together with the cathodes and anodes they must contact, explain how solid–solid interfaces form and degrade chemically, electrochemically, and mechanically, and critically assess the experimental techniques used to diagnose them. An area-specific resistance analysis indicates that once separators are about 30 μm thick and conductivities exceed ~1 mS cm^{-1}, interfacial and composite-electrode resistances, rather than bulk conductivity, usually dominate ohmic loss. Three 'translation gaps' are identified in which bulk metrics or computational descriptors (ionic conductivity, thermodynamic stability windows and elastic-modulus criteria) fail to predict cell behaviour. AI studies are graded on two complementary scales: the type of validation (Levels L1–L4) and the cell-level validation scale (grades A–D). Experimentally validated successes are concentrated in bulk properties and low-dimensional synthesis optimisation, whereas interface prediction remains largely computational, trained on small datasets and bounded by an experimental 'noise floor' (inter-laboratory relative standard deviations of 35–50% in the conductivity of identical samples). We propose an Interface Co-Design Framework with four operationally defined validity gates, chemical pairing, mechanical contact, transport translation, and manufacturing and safety validation, together with measurable reporting criteria and a Minimum Interface Data Record. AI is likely to accelerate practical solid-state batteries only if its training labels describe the failure modes that limit cells and if electrolyte, electrode, interface and processing are optimised jointly rather than sequentially.

1. Introduction

Commercial lithium-ion batteries rely on liquid electrolytes consisting of lithium salts dissolved in organic carbonates. These electrolytes conduct ions well and wet porous electrodes, but they are flammable, thermodynamically unstable both against lithiated graphite

* Corresponding author.
E-mail address: medtihtih@gmail.com (M. Tihtih).

https://doi.org/10.1016/j.rineng.2026.113995
Received 1 October 2026; Received in revised form 29 October 2026; Accepted 2 November 2026
Available online 4 November 2026
2590-1230/© 2026 The Authors. Published by Elsevier B.V. This is an open access article under the CC BY license (http://creativecommons.org/licenses/by/4.0/).

or lithium metal and against charged high-voltage cathodes, and they are consumed continuously by interphase formation during the life of the cell [1–3]. Under abuse conditions the electrolyte also participates in the exothermic sequence that leads to thermal runaway [4]. These limitations restrict both the safety margin and the use of high-capacity negative electrodes such as lithium metal [1–3].

Solid electrolytes (SEs) address these limitations in principle: they eliminate the need for a volatile fuel, they conduct only lithium ions, and they may enable lithium-metal or high-silicon anodes that increase energy density [1–3]. The discovery of sulfide conductors with room-temperature conductivities comparable to or higher than those of liquid electrolytes [5–7] removed what had long been regarded as the principal obstacle, and the chemical design space has since expanded to garnet, halide, and oxyhalide conductors [8–10].

The main SE classes offer different compromises (Fig. 1a). Oxides such as garnet $Li_7La_3Zr_2O_{12}$ are comparatively stable against lithium and tolerant of air but are stiff and require high-temperature processing [8,11,12]. Sulfides combine high conductivity with mechanical softness and cold-pressability, but their electrochemical stability windows are narrow, and they release H_2S on hydrolysis [3,13–15]. Halides tolerate 4 V-class cathodes without coatings but are reduced at low potentials [9,16]. Solid polymer electrolytes are processable and adhere well to electrodes, yet their room-temperature conductivity is limited unless liquids or fillers are added, thereby turning them into gels or composites with different safety and stability characteristics [3,17,18]. Polymer–ceramic composites attempt to combine the advantages of both families but introduce an internal polymer|ceramic interface [3,19]. Sodium-based solid-state systems follow the same logic with different chemistry and cost drivers [20,21].

Whatever the electrolyte class, the SE must form a working interface with two electrodes. Unlike a liquid, a solid electrolyte does not wet electrode surfaces: the interface is created during assembly by pressing, sintering, casting or in situ polymerisation, and it then evolves through chemical reaction, electrochemical decomposition at the electrode potentials, space-charge redistribution and mechanical contact loss as the electrodes change volume [22–26]. Fig. 1b summarises how bulk properties, interface formation, degradation and measurable cell performance are linked. Benchmarking studies show that all-solid-state batteries (ASSBs) still lag behind their energy and power targets [28], and the development challenges identified concern interfaces, microstructure, stack pressure and manufacturing rather than the ionic conductivity of the separator material [11,29]. SE|electrode interfaces are chemically and electrochemically unstable, mechanically unforgiving and difficult to characterise [22–24].

Interfacial stabilisation strategies, cathode coatings, interlayers, catholyte/anolyte multilayers, particle-size engineering and controlled stack pressure, have produced large, measurable gains. For example, an ultrathin atomic-layer-deposited Al_2O_3 layer reduced the room-temperature Li|garnet interfacial resistance from 1710 to 1 Ω cm^2 [12], and the critical stripping current of Li|Li_6PS_5Cl|Li cells increased from 0.2 to 1.0 mA cm^{-2} when the stack pressure was raised from 3 to 7 MPa [27]. Such results are, however, highly sensitive to test conditions. A study in which 21 groups used identical commercial materials found large variability in cell assembly and electrochemical performance [30], and an earlier round-robin study of identical argyrodite samples reported conductivity ranges of up to 4.5 mS cm^{-1} between laboratories [31]. The practical question is therefore which measurements can be trusted and which combinations of materials and

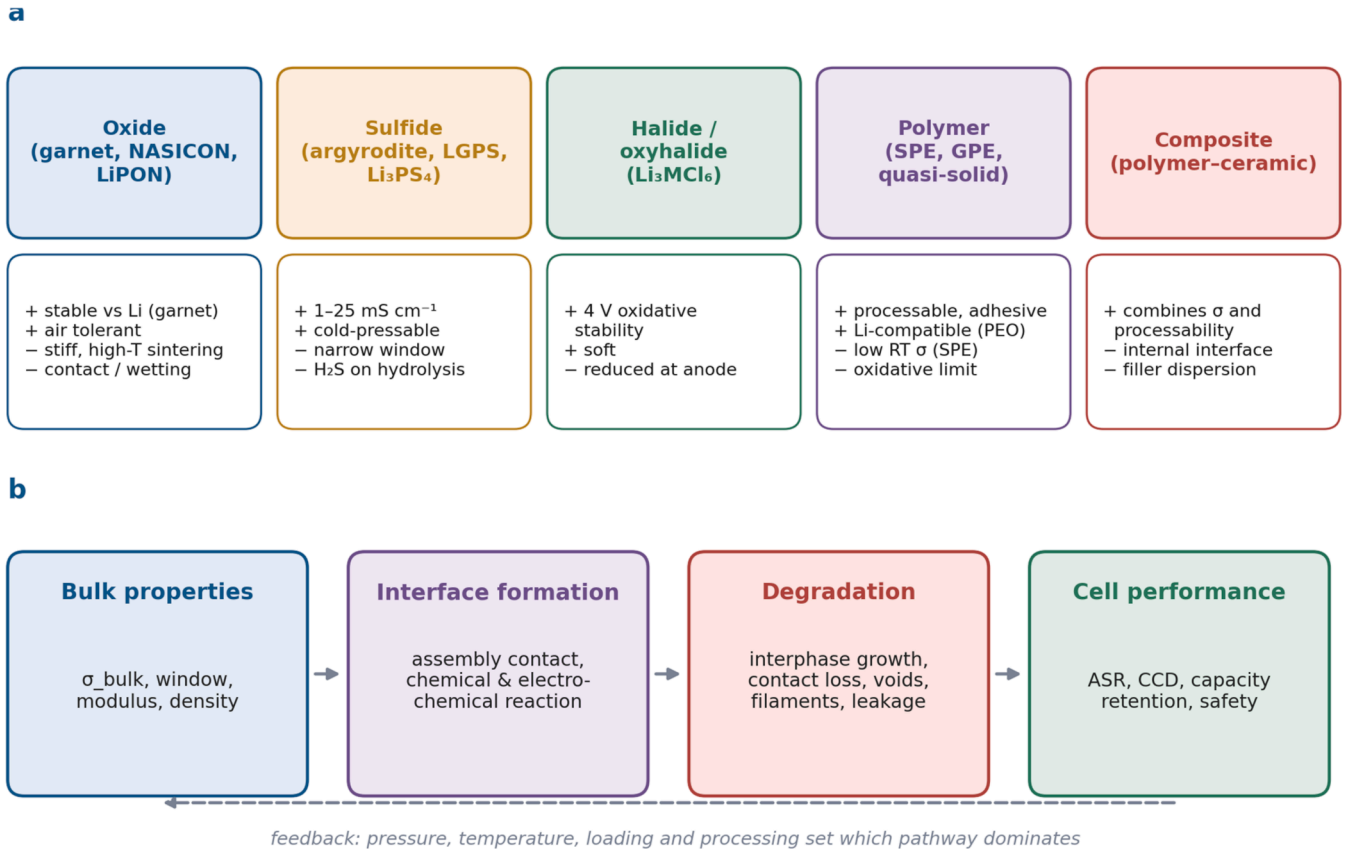


Fig. 1. Solid-electrolyte classes and the link between bulk properties, interface formation and cell performance. (a) Principal SE classes with representative advantages (+) and limitations (−); sources and conditions are given in Section 4. (b) Conceptual chain from bulk properties through interface formation and degradation to measurable cell metrics; pressure, temperature, loading and processing determine which pathway dominates. Original schematic based on refs [3,9,11–13,17,22–27].

processing should be built.

AI and machine learning (ML) are now being applied to this design problem at increasing scale. Graph networks have predicted millions of potentially stable crystals [32], AI-accelerated screening pipelines have narrowed tens of millions of candidates down to a few synthesised electrolytes [33], Bayesian optimisation has improved electrolyte synthesis routes with directly measured conductivity [34], and autonomous laboratories have begun to close the loop between prediction and synthesis [35]. At the same time, some 'discovered' compounds were found not to be new [36], the meaning of discovery at this scale has been questioned [37], and universal ML interatomic potentials have been shown to underestimate Li^+ migration barriers systematically [38]. The battery community has been encouraged to distinguish hype from reality in AI-driven research [39].

Several recent reviews address parts of this intersection: computational and ML methods for SEs [40,41], AI for SE and interface engineering [42], ML for SSB materials screening and state estimation [43], AI for rechargeable-battery materials [44], interface stability and interphases [22,23], battery mechanics [24], and the solvation-driven molecular design of polymer electrolytes, including the prospects of AI for sodium systems [21]. These reviews are thorough within their scope, but most are organised by material class or by method. Few start from the failure mechanisms that limit cells and ask whether the quantities that AI models are trained to predict are the quantities that limit those cells. Moreover, the strength of the evidence behind AI claims is rarely graded explicitly, although general reporting checklists for ML studies exist [45,46].

The knowledge gap addressed here is therefore the absence of an evidence-graded, interface-centred link between (i) materials chemistry and processing, (ii) the measurable interfacial quantities that control cell polarisation, degradation and safety, and (iii) the labels and validation standards used in AI-guided discovery.

This review has four objectives. First, it compares electrolytes and electrodes with the interface as the unit of analysis, including an expanded assessment of solid polymer, gel and composite electrolytes. Second, it critically evaluates the experimental techniques and quantitative metrics area-specific resistance (ASR), critical current density (CCD), pressure dependence, capacity retention, and thermal-abuse parameters—that determine whether an interface is fit for use in a cell. Third, it grades AI claims on two explicitly defined scales and identifies where data and labels limit progress. Fourth, it consolidates these findings into an Interface Co-Design Framework with four operationally defined validity gates. We do not claim that evidence grading, staged validation, or co-design are new concepts; analogous approaches exist in clinical guideline development [47] and in ML reporting checklists [45,46]. The contribution lies in adapting them to SSB interfaces, defining measurable pass/fail criteria and connecting them to the labels used by AI models (Section 2.4). This decision-oriented scope, which links materials chemistry, interface engineering, measurable electrochemical performance and manufacturing constraints, is consistent with the interdisciplinary engineering scope of Results in Engineering.

The review is organised as follows. Section 2 describes the methodology and the evidence-grading scheme; Section 3 re-examines safety; Sections 4–7 address electrolytes, electrodes, interfaces and interface engineering; Section 8 assesses characterisation techniques; Section 9 analyses three translation gaps quantitatively; Sections 10–12 grade AI applications and data limitations; Section 13 integrates theory, computation and experimental design; Section 14 presents the co-design framework and its operational criteria; and Section 15 discusses unresolved contradictions and future directions.

2. Scope, review methodology, evidence grading and position relative to existing reviews

2.1. Scope

The review covers lithium-based solid-state and hybrid batteries in which a solid electrolyte replaces the liquid electrolyte or assumes its primary function. It includes inorganic oxide, sulfide, halide and oxyhalide electrolytes; solid polymer, gel/quasi-solid and polymer–ceramic composite electrolytes; layered-oxide, polyanionic and (briefly) conversion cathodes; and lithium-metal, anode-free, silicon and alloy anodes. Sodium-based systems are discussed in Section 4.6, where they test whether lithium-based conclusions transfer. Electrolyte families are included only insofar as they support the central argument; the review is not intended to be a catalog.

2.2. Literature identification and selection

This is a critical, evidence-graded narrative review, not a systematic review: no protocol was registered, and the numbers of records retrieved and excluded at each stage were not logged in a form that would support a PRISMA-type flow diagram. We therefore report the selection procedure as transparently as the available records allow and distinguish two stages.

Original selection. The literature was restricted mainly to 2018–2026, with emphasis on 2022–2026; older publications were included when they established a concept, a measurement method or a material family. Search databases, search dates, and representative search strings were not recorded. Inclusion required that a study (i) concerned lithium-based SE, electrode or interface behaviour, or AI/ML applied to these; (ii) for quantitative or mechanistic claims, was a peer-reviewed primary study reporting the measurement or calculation conditions; and (iii) had a bibliographic record verifiable in publisher, repository or indexing records. Reviews were used for context and terminology, not as sources of specific results. Preprints were included only when no peer-reviewed equivalent existed and are labeled as such. Studies of liquid-electrolyte cells were excluded except as explicitly labeled contrasts.

Revision-stage verification and update (October 2026). During revision, targeted searches were conducted using a general web search engine to verify bibliographic records and identify additional primary studies requested by the reviewers. Representative queries combined terms such as 'polymer electrolyte' with 'ceramic nanowire filler', 'single-ion', 'in situ polymerization' or 'transference number'; 'critical stripping current'; 'stack pressure all-solid-state lithium metal'; 'thermal runaway sulfide all-solid-state'; 'impedance spectroscopy all-solid-state batteries'; and 'sodium solid electrolyte'. Records were checked against publisher landing pages, institutional repositories and indexing services. Screening was performed by the authors in a single pass; no inter-reviewer agreement statistic was computed, and no formal risk-of-bias tool was applied.

2.3. Data extraction and comparability rules

Numerical values in the text and tables are limited to those reported in the cited sources and are given with their measurement conditions (temperature, pressure, thickness, cell configuration) where available. Values that we calculated are identified as derived, and their equations and inputs are stated (Section 9.1). Values obtained under incompatible conditions are not pooled; differences smaller than the documented inter-laboratory spread are not interpreted [30,31]. Because protocols are heterogeneous, no meta-analysis was attempted; the synthesis is semi-quantitative.

Table 1
Landscape of the reviews most relevant to this work and the added value claimed here. Gaps are based only on the stated scope and structure of each review (not on judgments of quality): ●, central; ◐, partial; ◦, not a stated focus.

Review (year)	Main focus	Electrolytes	Electrodes	Interfaces	AI/ML	Gap relative to this review	Added value here
Famprikis et al. (2019) [48]	Fundamentals of inorganic SEs	●	◦	◐	◦	No AI; limited cell-level translation	Links bulk fundamentals to cell-level failure
Zhao et al. (2020) [3]	SE design for safe, energy-dense cells	●	◐	◐	◦	Safety premise not stress-tested	Evidence-based safety re-assessment
Xiao et al. (2020) [22]	Interface stability, computation vs experiment	◐	◐	●	◦	Thermodynamic emphasis; predates ML interface models	Thermodynamic vs kinetic gap as an AI label problem
Banerjee et al. (2020) [23]	Interphases with inorganic SEs	◐	◐	●	◦	No data or AI perspective	Interface data requirements (MIDR)
Janek & Zeier (2023) [29]	Development bottlenecks of SSBs	◐	◐	◐	◦	AI not addressed	Maps bottlenecks to AI evidence levels
Kalnaus et al. (2023) [24]	Mechanics of SSBs	◐	◐	●	◦	No AI; mechanics treated separately	Mechanics as a gate in co-design
Lombardo et al. (2022) [39]	AI across battery research	◐	◐	◐	●	Not SSB-interface-specific	SSB-interface-specific evidence grading
Zheng, Zhou & Zhu (2024) [40]	First principles to ML for SEs	●	◦	◐	●	Electrode side and cell metrics limited	Electrode–electrolyte co-design
Dutra et al. (2025) [41]	Atomistic modelling and ML of inorganic SEs	●	◦	◐	●	Computation-centred; experiment/cell not focal	Computation–experiment noise floor
Wang, Zeier & You (2025) [42]	AI for SE and interface engineering	●	◐	●	●	Electrode co-design, safety and evidence grading not stated foci	Four-gate framework; label validity
Wang et al. (2025) [43]	ML for SSB materials and BMS	◐	◐	◦	●	Interface mechanisms not focal	Mechanism-first organisation
Hu et al. (2025) [44]	AI for rechargeable battery materials	◐	●	◦	●	Broad; SSB interfaces not organising theme	Interface-centred synthesis
AI Agent review (2025) [50]	AI agents for SEs	●	◦	◐	●	Electrolyte-centred	Cell-level validation gates
Kwak et al. (2022) [16]	Halide superionic conductors	●	◐	◐	◦	Single family	Cross-family trade-off analysis
Kala et al. (2026) [21]	Solvation and molecular design of SPEs for Na-metal batteries	● (polymer)	◐	◐	◐ (prospective)	Na-specific; AI as a future direction	Cross-family gates; graded AI evidence; Li/Na transfer limits

Table 2
Contribution audit: what this review reorganises and what it adds.

Element	Precedent in the literature	Reorganised from existing work	New in this review	Status / limitation
Interface as unit of analysis	Interface and interphase reviews [22,23]; bottleneck analyses [29]	Interphase, contact, void and leakage mechanisms	Mechanism-indexed comparison across electrolyte and electrode families with diagnostic signatures (Sections 5–7)	Synthesis of published data
Safety re-assessment	Thermal studies of SE–electrode reactions and cells [51–57]	Runaway pathways	Removed/retained/introduced classification and measurable reporting set (Section 14)	Thresholds remain chemistry-specific
Translation gaps	Individual observations on σ vs ASR [12,58], windows vs passivation [26,59], modulus vs flaws [60,61]	Underlying observations	Pairing of each gap with the AI label it corrupts and a gate-aware replacement; ASR budget (Section 9.1)	Calculations are illustrative
Evidence grading	GRADE [47]; ML reporting checklists [45, 46]	Concept of graded evidence	Two-axis scheme (L1–L4 × A–D) with crosswalk for SSB claims (Section 2.5)	Assigned by the authors; not independently replicated
Noise floor	Inter-laboratory studies [30,31]; uMLIP softening [38,62]	Spread and bias values	Use of inter-laboratory spread as minimum meaningful model error; comparison with method bias (Section 12)	Based mainly on argyrodites
Four validity gates	Stage-gate decisions common in engineering development	Bottleneck categories [24,29]	Pass/conditional/fail/insufficient states, anchor values and decision rule (Section 14)	Proposed; not yet prospectively tested
MIDR	Reporting parameters proposed in [30]; ML checklists [45]	Reporting variables	Interface-specific minimum record (Box 1)	Proposed standard

2.4. Position relative to existing reviews and contribution audit

The reviews most relevant to the present work are summarised in Table 1. The fundamentals of electrolyte chemistry are covered extensively [3,48,49]; interface stability [22,23], battery mechanics [24] and development bottlenecks [29] are well reviewed; AI for batteries in general [39,44] and the computation-driven design of SEs [40,41] are well covered; and solvation-based design of polymer electrolytes has recently been reviewed for sodium-metal batteries [21]. The two most recent works on AI and atomistic modelling [41,42] address electrolytes and interfaces, respectively. The present review differs in organisation rather than in topic list: failure mechanisms form the main axis, the electrode side of the interface is treated with the same mechanistic depth, AI evidence is graded explicitly, and a co-design framework is derived from the gap between model predictions and cell requirements.

The novelty of the present contribution is examined critically in Table 2, which separates elements that reorganize existing findings from elements that are new in this review. Most of the mechanistic content is a critical synthesis of published work; the new elements are the explicit two-axis evidence grading, the pairing of each translation gap with a

Table 3
Unified evidence-grading scheme used in this review. Crosswalk: L2–L4 ⇒ D; L1 ⇒ A, B or C. Grades are ordinal, not cardinal, and were assigned by the authors.

Grade	Applies to	Definition and criteria	Required evidence	Meaning of uncertainty	Example (refs)	Limitation
L1	AI / computational claim	Prediction or decision confirmed by synthesis or measurement	Prospective experiment on the predicted item	Residual: measurement noise floor, single-laboratory replication	Bayesian-optimised Li$_3$SiPS$_4$ synthesis [34] (L1/C); AI + HPC screening with synthesis [33] (L1/C)	Does not indicate cell relevance; combine with A–D
L1 (contested)	AI claim	L1 claim challenged in a published analysis	Original claim + published critique	Validity of the confirmation itself is disputed	Autonomous synthesis [35] vs critique [36]	Depends on critiques being published
L2	AI / computational claim	Agreement with DFT/AIMD or retrospective data only	Benchmark against computational reference or held-out data	Dominated by reference-method bias and transfer to experiment	AIMD-trained reactivity classifier [59]; uMLIP vs DFT [38,62]	Retrospective tests can hide data leakage
L3	AI / computational claim	Plausible and proposed, not demonstrated	Published proposal or concept	Plausibility only	ML-extended coating screening [63,64]	Subjective boundary with L2
L4	Target property	No convincing evidence found	,	Absence of evidence in reviewed literature, not evidence of absence	AI for experimental CCD or interfacial ASR	Sensitive to search coverage (Section 2.6)
A	Any claim or strategy	Full cells at practical loading, several groups	Independent full-cell reports with stated loading	Scale-up and manufacturing remain	None of the strategies reviewed in Section 7 currently meets A	'Practical loading' is application-dependent
B	Any claim or strategy	Full cells under laboratory conditions	Full-cell cycling data	Laboratory pressure, temperature or loading may hide failure modes	Halide catholyte [65]; Ag–C anode-free cells [66]; μSi|sulfide [67]	Broad category
C	Any claim or strategy	Symmetric, half, model cells or component-level data	Symmetric/half-cell or pellet measurements	Current-focusing cascade (Section 6.7) not tested	Stack-pressure control in symmetric cells [27]	Cannot reveal electrode crosstalk
D	Any claim or strategy	Computational or proposed only	Calculation or proposal	No experimental test	Coating screening before validation [63]	Includes all L2–L4 claims

replacement AI label, the quantitative resistance budget and the operational gate criteria. These new elements are proposals and have not yet been tested prospectively.

2.5. Evidence grading: two complementary scales

Two scales are used throughout, and they measure different properties (Table 3). The **evidence level (L1–L4)** grades the type of validation that an AI or computational claim has received. **Level 1** (experimentally demonstrated): an AI prediction or decision was followed by synthesis or measurement that confirmed it. **Level 2** (computationally demonstrated): good performance against computational reference data such as density functional theory (DFT) or ab initio molecular dynamics (AIMD), without experimental testing or with only partial testing. **Level 3** (conceptually proposed): the application is scientifically plausible and has been proposed but not convincingly demonstrated. **Level 4** (open opportunity): no convincing evidence was found in the literature reviewed. Where a claim has been publicly challenged with evidence, both the claim and the challenge are reported ('contested'), and claims available only as preprints are marked 'provisional'.

The **validation-scale grade (A–D)**, grades the most demanding configuration in which any claim, AI-derived or not, has been tested: **A**, full cells at practical loading reported by several groups; **B**, full cells under laboratory conditions; **C**, symmetric, half, model cells or component-level measurements (for example, pellet conductivity); **D**, computational or proposed only. The two scales are linked by a crosswalk: an L2–L4 claim carries grade D by definition, whereas an L1 claim carries A, B, or C according to how it was validated. AI claims are therefore reported in combined notation (e.g., L1/C), and interface-engineering strategies that are not AI-derived receive only an A–D grade. Neither scale is redundant: two L1 claims can differ greatly in practical relevance (L1/A versus L1/C), and two strategies with grade B can rest on different kinds of evidence.

2.6. Limitations of the approach and representativeness

Because the selection was not systematic, the absence of a study in this review cannot be interpreted as a lack of literature on the topic. Three biases may affect the conclusions on AI. First, the selection favours high-visibility, English-language journals, so successful applications are likely to be over-represented relative to unsuccessful ones; this would make the published evidence appear stronger than it is, and it does not weaken our conclusion that interface prediction is immature. Second, industrial or unpublished datasets may contain interface data that are not visible to us, so a Level 4 grade means that no convincing evidence was found in the reviewed literature, not that such a capability does not exist. Third, the grades were assigned by the authors; Table 3 states the criteria so that readers can re-grade individual studies.

3. Does replacing the liquid electrolyte remove the hazard?

The safety case for solid electrolytes appears straightforward: if the carbonate electrolyte is the main fuel in lithium-ion thermal runaway, removing it should remove the fire. In liquid-electrolyte cells, runaway proceeds through a well-defined sequence of exothermic processes, interphase decomposition, anode–electrolyte reactions, cathode oxygen release and electrolyte combustion, that is often triggered by an internal short circuit [4]. Replacing the electrolyte interrupts some, but not all, of these steps, and the available evidence now allows the premise to be tested rather than assumed (Fig. 2).

Three lines of evidence qualify the premise. First, oxide SEs regarded as thermally robust can become oxygen sources at high temperatures: combined calculations and experiments indicate that oxygen release from common SEs in contact with molten lithium can be strongly exothermic and lead to thermal runaway, with interfacial properties

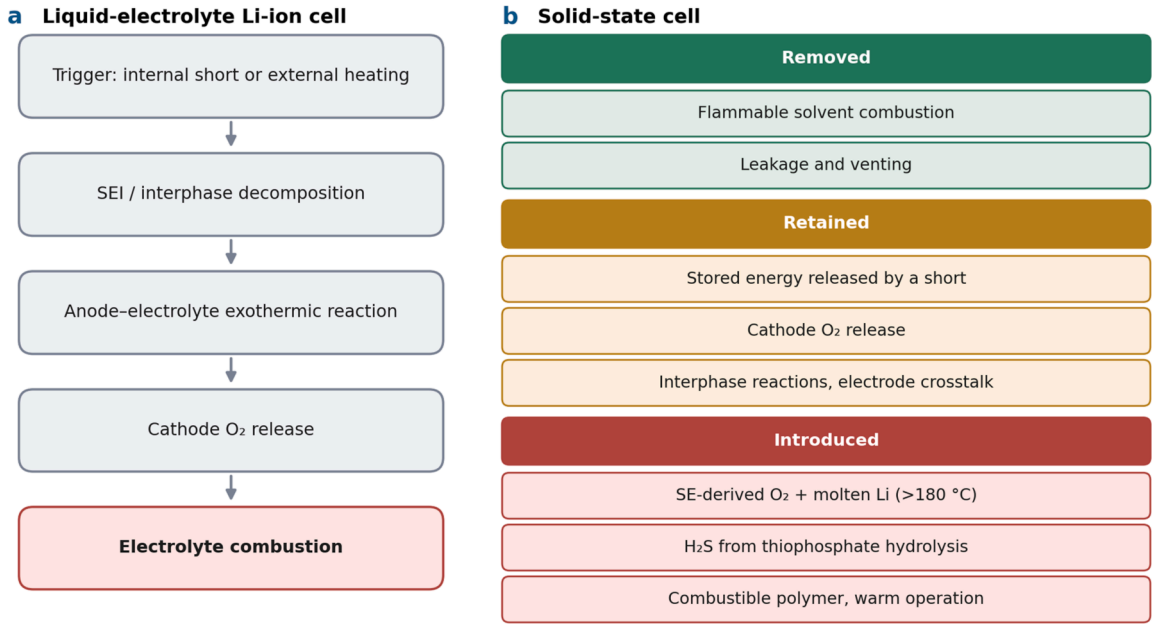


Fig. 2. Hazards that solid electrolytes remove, retain or introduce. (a) Thermal-runaway sequence of a liquid-electrolyte lithium-ion cell. (b) Corresponding pathways in solid-state cells, grouped as removed (flammable solvent, leakage), retained (energy released by an internal short, cathode oxygen release, interphase reactions and crosstalk) or newly introduced (reaction of SE-derived oxygen with molten lithium, H_2S from thiophosphate hydrolysis, combustible polymer requiring warm operation). Original schematic; the evidence type for each pathway is given in the text and in Section 14. Based on refs [3,4,51,53–57].

modulating the outcome [51]. Significant exothermic events had previously been detected in ASSB microcells by differential scanning calorimetry (DSC) [52]. Second, sulfide-based cells have their own runaway pathways [53]: in DSC experiments, crystalline sulfide SEs remained stable against the lattice oxygen released by charged Ni-rich cathodes at 200 °C but reacted with the cathode decomposition products at 300 °C, and gas–solid reactions with released oxygen were identified as a distinct pathway [53]. Sulfide SEs also react thermally with lithium metal [54], and the release of cathode oxygen was identified as the cause of runaways in ampere-hour-scale solid-state lithium-metal pouch cells [55]. Modeling and experiments further indicate that interphases and chemical crosstalk between the electrodes, rather than the electrolyte alone, determine the thermal stability of solid-state cells [56]. Third, thermodynamic models of failure scenarios showed that ASSBs are not inherently safe: a short-circuited all-solid-state cell with a $Li_7La_3Zr_2O_{12}$ electrolyte can reach temperatures significantly higher than a conventional lithium-ion cell, whereas adding a small amount of liquid electrolyte to the cathode increases heat release only in specific failure scenarios [57]. Large-format modeling of lithium-metal ASSBs under thermal-ramp and short-circuit conditions points in the same direction [68]. Stack pressure, an operating variable specific to solid-state cells, also affects the thermal-runaway behaviour of pellet-pressed $LiNi_{0.8}Co_{0.1}Mn_{0.1}O_2|Li_6PS_5Cl$ composite cathodes [69].

Two further hazards are specific to solid-state chemistries. Because lithium melts at approximately 180 °C, any design with a lithium-metal anode turns a mechanical failure (a filament or a cracked separator) into a risk of molten lithium contacting an oxygen-releasing cathode. Thiophosphate electrolytes hydrolyse in humid air and release H_2S, which requires dry-room processing and introduces a toxic-gas hazard that does not exist in liquid-electrolyte processing [3]. Polymer electrolytes are organic and combustible; without volatile solvents they reach practically useful conductivities only above ambient temperature (Section 4.4) [3,17].

The key conclusion is that non-flammability is a material property, whereas safety is a cell property that depends on stored energy, interphase chemistry and cathode–anode crosstalk. Solid electrolytes can eliminate the dominant fuel and widen the temperature tolerance window, but they do not remove the need for abuse testing of complete cells, and a higher energy density increases the energy that a short circuit can release. Material-level DSC or flammability tests are therefore not sufficient proof of safety. The measurable safety parameters and the conditions under which they should be reported are summarised in Section 14 (Gate 4 and the associated safety metrics).

4. Solid electrolytes: what bulk metrics reveal and what they hide

4.1. Oxides

Doped garnet-type $Li_7La_3Zr_2O_{12}$ (LLZO) compositions reach conductivities approaching 1 mS cm^{-1} and appear stable against lithium metal [8,12]; LLZO has therefore become the reference oxide for lithium-metal cells. Its main limitations are interfacial and processing-related rather than intrinsic. Lithium does not wet air-exposed garnet surfaces, and the as-assembled Li|garnet interface can show an area-specific resistance of the order of 10^3 Ω cm^2 (1710 Ω cm^2 at room temperature in ref [12]), which an ultrathin Al_2O_3 interlayer that enables wetting reduced to ~1 Ω cm^2 [12]. Surface contamination, lithium penetration along grain boundaries, and degradation during storage remain common problems [70,71], and lithium nucleation inside the ceramic caused by electronic conductivity or local electronic structure is a further risk [72,73]. Densification normally requires high sintering temperatures, which complicate lithium retention and co-processing with cathodes; sinter-free designs and all-ceramic composite cathodes have been developed in response [74–76], but manufacturing robust separators as thin as polymer membranes remains a central challenge [11]. NASICON phosphates are air-stable and resistant to oxidation, but their reducible Ti^{4+} or Ge^{4+} cations make them unstable against lithium, whereas LiPON thin films conduct poorly but are kinetically stable and resist lithium penetration [48,72]. The oxide family thus illustrates the first principle of this review: thermodynamic stability does not guarantee a working interface, because contact, wetting and electronic leakage at the interface determine cell behaviour.

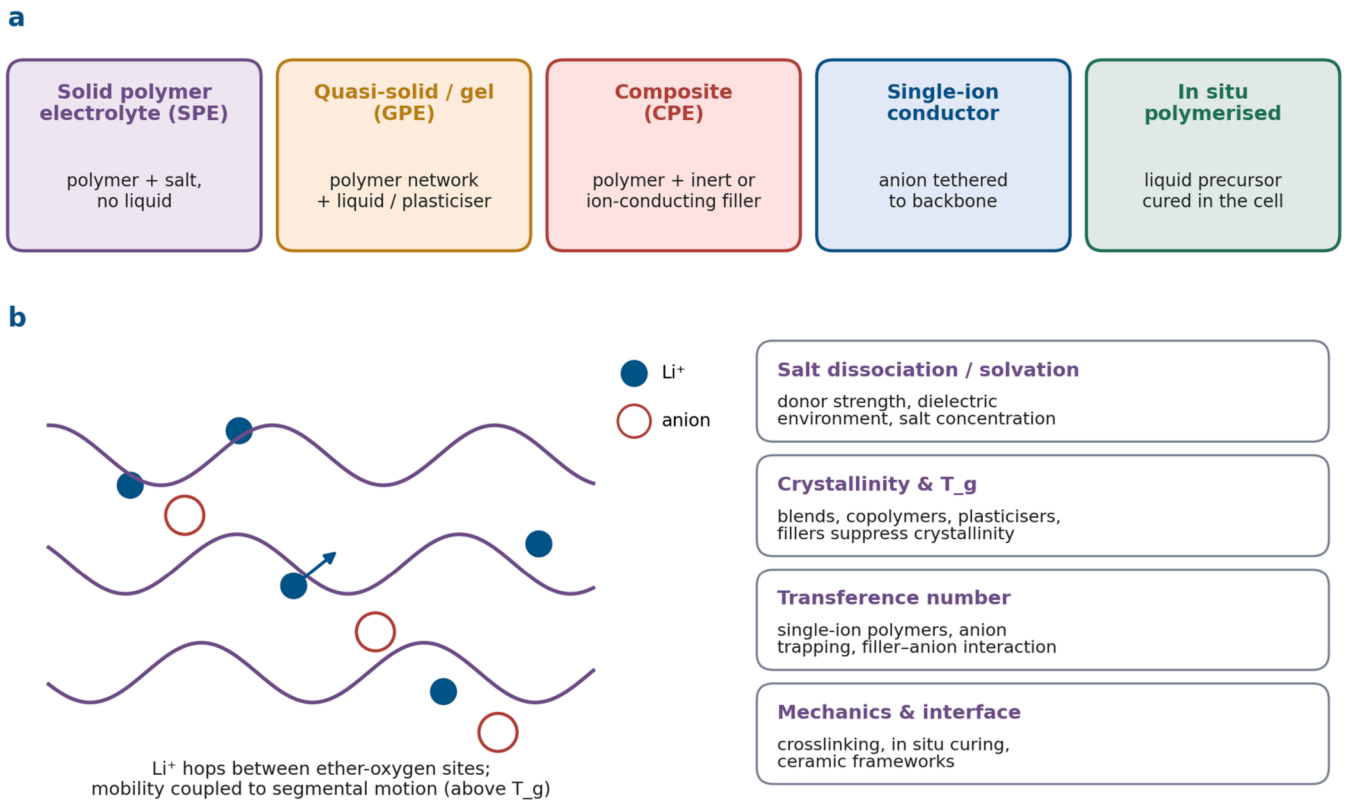


Fig. 3. Polymer-based electrolytes. (a) Principal classes; gel/quasi-solid electrolytes contain a liquid phase and are not interchangeable with solvent-free SPEs. (b) Schematic of Li^+ transport coupled to the segmental motion of a polyether host, and the main design levers. Original schematic based on refs [3,17–19,21,83–85].

Table 4
Polymer-based electrolyte classes: composition, transport mechanism, reported performance (with conditions), engineering advantages, limitations and characterisation methods. Values are as reported in the cited studies and are not directly comparable across rows.

Class	Composition / structure	Dominant transport mechanism	Reported performance (conditions)	Advantages	Limitations	Key characterisation
SPE (PEO–Li salt)	Salt in solvating polyether, no liquid	Li^+ hopping coupled to segmental motion above T_g	~10^{-5} S cm^{-1} at 30 °C with nanofillers [17]; t_+ 0.46 (a.c./d.c., 90 °C) vs 0.06 (Hittorf) [86,87]	Solvent-free, processable, adhesive, Li-compatible	Low RT σ; low t_+; oxidative limit	EIS, DSC (T_g, crystallinity), XRD, transference, LSV
Alternative hosts, blends, copolymers	Polycarbonates, polyesters, block copolymers	Weaker coordination; decoupled mechanics	Host-dependent [18]	Tunable crystallinity and modulus	Synthesis complexity; fewer stability data	DSC, DMA, FTIR/Raman (coordination)
Single-ion conductor	Anion tethered to backbone	Cation-only migration; $t_+ \rightarrow 1$	~10^{-4} S cm^{-1} at 70 °C; $t_+ \approx$ 0.91; 4 V window [84]	Less concentration polarisation	Low RT σ; elevated-T operation	EIS, transference (method stated), LSV
GPE / quasi-solid	Liquid or plasticiser in polymer network	Liquid-like transport in swollen domains	Near-liquid σ [3]	RT operation; good wetting	Flammability and volatility partly reintroduced; weaker mechanics	TGA (liquid content), flammability, EIS
CPE, inert filler	SiO_2, TiO_2, Al_2O_3 in PEO	Crystallinity suppression; Lewis acid–base interactions	4.4×10^{-5} (30 °C), 1.2×10^{-3} S cm^{-1} (60 °C) [83]	Better mechanics and σ	Dispersion and agglomeration	XRD, DSC, SEM/TEM
CPE, ion-conducting filler	e.g., LLTO nanowires in PAN	Transport along percolating filler surfaces	2.4×10^{-4} S cm^{-1} at RT (15 wt%) [19]	Higher σ; wider window	Polymer|ceramic interface; filler stability	EIS, solid-state NMR, tomography
In situ polymerised	Liquid precursor cured in the cell (e.g., poly-DOL)	Conformal contact; fast interfacial transport	Demonstrated in Li cells [85]	Low interfacial resistance; manufacturable	Conversion, residual monomer, oxidative stability	FTIR/NMR (conversion), EIS, TGA
Na SPEs	Polymer hosts with Na salts	Analogous; Na^+ solvation differs	Reviewed in [21]	Abundant elements	Low RT σ; Na-metal interface	As above; Na-specific interphase analysis

4.2. Sulfides

The field was transformed by the discovery that thiophosphate conductivities can match or exceed those of liquid electrolytes. A Si–Cl-substituted LGPS-type conductor reached 25 mS cm^{-1} and enabled high-power cells with low internal resistance, including operation at 100 °C [7], and glass-ceramics outperformed liquid electrolytes in cells [6]. Argyrodites Li_6PS_5X are now the workhorse materials [13], and halide

enrichment enhances their diffusivity [77]. Their mechanical softness allows cold pressing and yields low grain-boundary resistance, a processing advantage that no oxide currently matches.

Their weaknesses are electrochemical and environmental. Thiophosphates have narrow thermodynamic stability windows: they are oxidised at layered-oxide cathode potentials and reduced by lithium [14,15]. Whether the resulting interphases passivate depends on composition. LGPS-type phases containing reducible Ge form mixed-conducting interphases against lithium whose growth increases the cell resistance, as shown by in situ X-ray photoelectron spectroscopy combined with time-resolved impedance measurements [78], whereas some argyrodites form self-limiting interphases (Section 6). Cathode coatings are therefore required in sulfide cells [25,79], and the moisture sensitivity of sulfides requires dry processing [3]. Finally, reported conductivities carry large uncertainties: identical argyrodite samples measured in different laboratories gave total conductivities of 1.3–5.8 mS cm^{-1} for the most conductive sample, with relative standard deviations of 35–50% across all samples, and activation energies of 198–326 meV (relative standard deviation 5–15%) [31]. Differences in bulk conductivity smaller than this spread are not significant between laboratories.

4.3. Halides and oxyhalides

Chloride and bromide conductors (Li_3YCl_6, Li_3YBr_6) reopened the oxidative side of the stability question: they combine good conductivity with compatibility with uncoated 4 V-class cathodes [9]. Li_3InCl_6 offers tolerance to ambient air [80], chloride catholytes have enabled high areal capacity, long-life 4 V ASSBs [65], and Zr-based chlorides reduce dependence on rare metals [16,81]. Oxyhalides such as $LiNbOCl_4$ and $LiTaOCl_4$ exceed 10 mS cm^{-1} [10]; $LiNbOCl_4$ has a bulk modulus of only 22.7 GPa, which structural analysis attributes to framework flexibility and disorder [82]. The weakness of halides is reductive: most metal halides are reduced at lithium or silicon anode potentials, so halide cells are usually built as bilayers with a halide catholyte next to the cathode and a sulfide or other anolyte next to the anode. This solves one interface by creating another, and long-term evidence regarding the chemical and moisture stability of oxyhalides and the halide|sulfide junction remains limited.

4.4. Solid polymer, gel/quasi-solid and composite polymer electrolytes

Terminology and classification. Polymer-based electrolytes form a large and heterogeneous family whose classes are not interchangeable (Fig. 3, Table 4). Solid polymer electrolytes (SPEs) consist of a lithium salt dissolved in a solvating polymer host, typically a polyether such as poly(ethylene oxide) (PEO), without a liquid component [3,18]. Gel polymer electrolytes (GPEs) immobilise a liquid electrolyte or plasticiser in a polymer network; their conductivity approaches that of the liquid, but so do their flammability and electrochemical limitations, so they are quasi-solid rather than solid [3]. Composite polymer electrolytes (CPEs) disperse inert ceramic fillers (e.g., SiO_2, TiO_2, Al_2O_3) or ion-conducting ceramics in a polymer matrix [17,19,83]. Single-ion conducting polymers tether the anion to the polymer backbone [84], and in situ polymerised electrolytes are formed inside the assembled cell from a liquid precursor [85]. In this review, 'solid' denotes the absence of a free liquid phase; because residual solvent from solution casting alters both conductivity and stability, its content should be quantified and reported.

Ion transport, salt dissociation and solvation. In PEO-based SPEs, Li^+ is coordinated by ether oxygens and moves by hopping between coordination sites, a process coupled to the segmental motion of the amorphous phase above the glass-transition temperature (T_g) [3,18]. The conductivity is therefore governed by the amorphous fraction, by T_g, by the degree of salt dissociation and by the concentration of mobile ions. Because crystalline PEO domains conduct poorly, PEO–lithium-salt electrolytes reach ~10^{-4} S cm^{-1} only above ambient temperature; nanoscale ceramic fillers that kinetically inhibit crystallisation raised the conductivity near 30 °C to ~10^{-5} S cm^{-1} [17]. Salt dissociation and ion solvation depend on the donor strength and local dielectric environment of the coordinating groups and on salt concentration; a recent review of polymer electrolytes for sodium-metal batteries treats these effects explicitly as solvation-structure design principles linking ion coordination, salt dissociation and interfacial stability [21].

A key limitation of salt-in-polymer electrolytes is a low cation transference number: Li^+ is strongly coordinated while the anion moves more freely, so a large fraction of the current is carried by anions and concentration polarisation develops. The measured value depends on the method. A combined a.c./d.c. polarisation method gave 0.46 ± 0.02 for PEO–$LiCF_3SO_3$ at 90 °C [86], whereas a Hittorf measurement on an amorphous PEO–$LiClO_4$ electrolyte gave 0.06 ± 0.05 and indicated that steady-state polarisation and NMR methods can overestimate this parameter [87]. Transference numbers obtained by different methods, or for different salts and temperatures, should therefore not be compared directly.

Design levers and their trade-offs. Polymer blends, copolymers and alternative hosts such as polycarbonates, polyesters and polynitriles reduce crystallinity or weaken Li^+–polymer coordination, and block copolymers can decouple mechanical and transport functions by combining a conducting block with a rigid block [18]. Single-ion conductors raise the transference number by immobilising the anion: PEO-based triblock copolymers with tethered sulfonamide anions reached ~10^{-4} S cm^{-1} at 70 °C with $t_{Li+} \approx 0.91$ and a 4 V stability window, but cycling still required 70 °C [84]. Plasticisers and ionic liquids increase segmental mobility and conductivity but move the material towards the gel category, reducing mechanical strength and potentially reintroducing volatility or flammability [3]; their content should therefore be reported. Inert nanoparticle fillers suppress crystallisation and may promote salt dissociation through Lewis acid–base interactions [17]: SiO_2 nanospheres synthesised in situ in PEO gave 4.4×10^{-5} S cm^{-1} at 30 °C and 1.2×10^{-3} S cm^{-1} at 60 °C [83]. Ion-conducting $Li_{0.33}La_{0.57}TiO_3$ nanowires (15 wt%) raised the room-temperature conductivity of polyacrylonitrile–$LiClO_4$ from 2.1×10^{-7} to 2.4×10^{-4} S cm^{-1}, an effect attributed to fast transport along the nanowire surfaces [19]; filler morphology and percolation therefore matter as much as filler chemistry, and the polymer|ceramic interface becomes an internal design variable [3]. Crosslinking and network formation improve mechanical integrity and dimensional stability, generally at the expense of segmental mobility [18]. Porous polymer hosts made with pore-forming agents provide scaffolds for liquid or ionic-liquid uptake; such systems are gels and should be classified as such. Finally, in situ polymerisation forms the electrolyte inside the cell and produces conformal contact with electrode particles: $Al(OTf)_3$-initiated ring-opening polymerisation of 1,3-dioxolane yielded solid-state polymer electrolytes with fast interfacial transport [85].

Processing. Preparation routes include solution casting, solvent-free hot pressing or melt processing, and in situ polymerisation or curing inside the cell [3,85]. Solvent-free routes avoid residual solvent but require thermally stable salts; solution casting is simple but leaves solvent traces that should be quantified, for example by thermogravimetric analysis; in situ curing improves contact but requires control of conversion and of initiator or monomer residues.

Electrochemical stability and electrode interfaces. Polyethers have limited oxidative stability, which prevents pairing with higher-voltage cathodes such as $LiCoO_2$ unless protective catholytes are used [3]; $LiFePO_4$ is therefore the most common partner (Section 5.1). Against lithium metal, PEO-based SPEs are comparatively compatible and adhesive, but their low modulus offers little mechanical resistance to filament growth (Section 9, Gap 3) [61]. Interfacial resistance with porous electrodes can be lower than for rigid ceramics because the polymer can penetrate the electrode or be cured inside it [85].

Unresolved trade-offs. The polymer family illustrates a recurring trade-off: levers that increase ionic mobility (plasticisers, low T_g, high salt content) tend to reduce mechanical strength or electrochemical

Table 5
Comparison of solid-electrolyte families on the properties that determine cell behaviour. Unless stated otherwise, conductivities refer to room temperature; 'practical' stability is defined by cell behaviour and can differ from the thermodynamic window (Section 6.2).

Family (examples)	RT σ (reported)	vs Li / low-potential anodes	vs 4 V cathodes	Mechanics & processing	Air / moisture	Dominant interfacial failure	Key refs
Garnet oxide (doped LLZO)	approaching 10^{-3} S cm^{-1}	Kinetically stable; wetting-limited	Reactive during co-sintering	Stiff; high-T sintering; thin separators difficult	Carbonate/ hydroxide surface layers	Contact loss, voids, filaments via GBs/ electronic leakage	[8,11, 12, 72]
NASICON (LATP, LAGP)	moderate (sub-mS cm^{-1})	Unstable (reducible Ti^{4+}/Ge^{4+})	Robust	Stiff; sintering required	Stable	Reduction at anode; indirect decomposition	[26, 48]
LiPON (thin film)	~μS cm^{-1} (order)	Kinetically stable; resists Li penetration	Moderate	Vacuum deposition only	Moderate	Low σ limits thickness	[48, 72]
Thiophosphate / argyrodite (Li_6PS_5X)	10^{-3}–10^{-2} S cm^{-1}; inter-lab spread 1.3–5.8 mS cm^{-1} on one sample	Forms interphase; passivation composition-dependent	Oxidised; coating needed	Soft; cold-pressable	H_2S on hydrolysis	Cathode-side oxidation; contact loss	[13, 25, 31, 77]
LGPS-type	~10^{-2} S cm^{-1} (12–25 mS cm^{-1})	Reduced (Ge); mixed-conducting interphase	Oxidised	Soft	Sensitive	Anode-side reduction	[5,7, 15, 78]
Halide (Li_3MCl_6, Li_2ZrCl_6)	~10^{-4}–10^{-3} S cm^{-1}	Reduced; anolyte needed	4 V-compatible without coating	Soft; cold-pressable	Composition-dependent (In-based air-tolerant)	Anode-side reduction; bilayer junctions	[9,16, 65, 80]
Oxyhalide ($LiNbOCl_4$, $LiTaOCl_4$)	> 10^{-2} S cm^{-1}	Reduced (expected)	Evidence limited	Very soft (B ≈ 22.7 GPa for $LiNbOCl_4$)	Evidence limited	Evidence limited	[10, 82]
PEO-based polymer	~10^{-4} S cm^{-1} only above ambient temperature	Compatible	Limited (low-voltage cathodes)	Film-castable; adhesive	Moderate	Oxidation at high voltage; low RT σ	[3, 17]
Polymer–ceramic composite	intermediate (filler-dependent; 2.4 × 10^{-4} S cm^{-1} at RT reported for LLTO-nanowire/PAN)	Generally compatible	Limited to moderate	Processable	Moderate	Polymer|ceramic internal interface	[3,17, 19, 83]

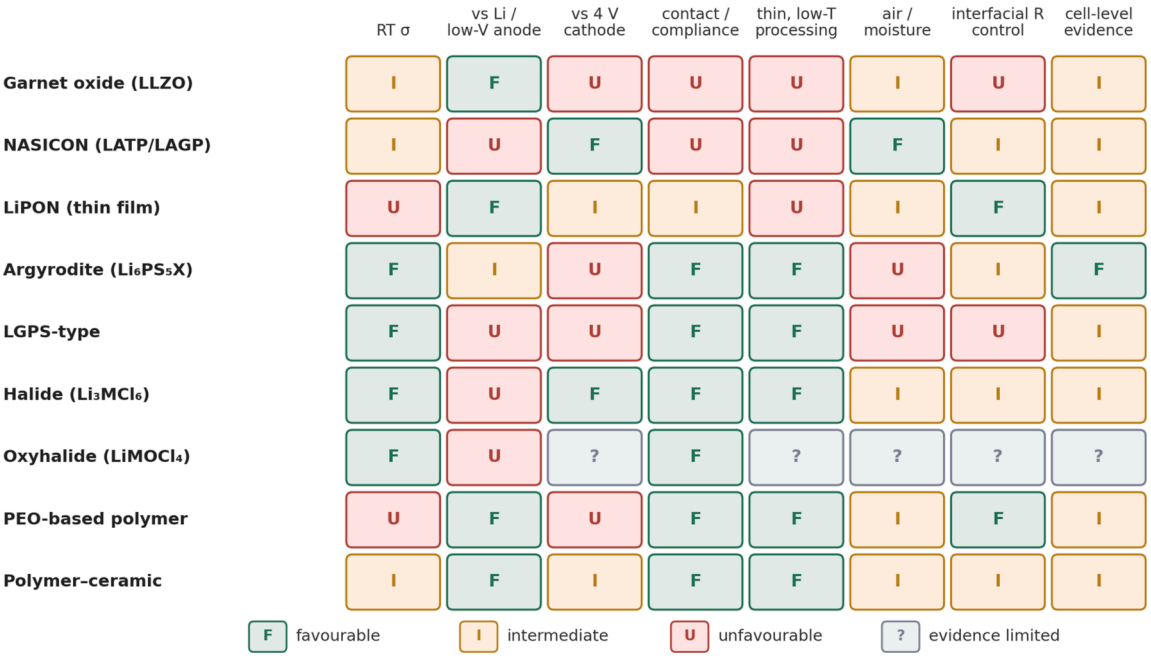


Fig. 4. Trade-off map of solid-electrolyte families. Qualitative assessment (favourable, intermediate, unfavourable, evidence limited) against eight criteria that determine cell performance and manufacturability. The map is a consensus-level synthesis of Table 5 and refs [3,9,10,17,22,31,48]; it is intended for comparing trade-offs, not for quantitative ranking.

stability, whereas levers that raise the transference number or strength (anion tethering, crosslinking, rigid fillers) tend to reduce conductivity. Because the experimental literature on polymer electrolytes is comparatively large, AI methods have been explored more extensively for polymers than for inorganic interfaces (Section 10.4) [88,89]. However, AI is presented mainly as a future direction in a recent review of sodium polymer electrolytes [21], and we found no prospectively validated AI design of a complete polymer electrolyte–electrode interface.

4.5. *Cross-family synthesis: the trade-off that forces multilayer designs*

Table 5 and Fig. 4 summarise the comparison. No family is

favourable on every criterion. Soft conductors, thiophosphates, halides, oxyhalides and polymers, are easy to densify and make good contact, but each has a limited stability range at one electrode or is sensitive to the environment; stiff oxides can be stable and air-tolerant but are difficult to process thin and to contact intimately. The practical response has been architectural: separate catholyte, separator and anolyte layers are selected so that each faces only the interface it can tolerate [65,81]. This is rational, but it increases the number of interfaces, each with its own chemistry, mechanics and processing window. The electrolyte question therefore becomes an interface question, and optimising one layer in isolation can shift the limiting process to an adjacent layer.

4.6. Beyond lithium: sodium solid-state systems and the limits of transferability

Sodium-based solid-state batteries are a prominent post-lithium option because sodium is abundant and inexpensive. Sulfide sodium conductors were established early: a glass-ceramic electrolyte containing cubic Na_3PS_4 reached 2×10^{-4} S cm^{-1} at room temperature and enabled room-temperature operation of an all-solid-state sodium cell [20]. Solid polymer electrolytes for sodium-metal batteries face the same low room-temperature conductivity, interfacial incompatibility with the metal and poor electrode contact as their lithium counterparts, and solvation-structure design has been proposed as the organising principle for their development [21]. Some lithium-derived mechanisms appear to transfer: void formation above a critical stripping current, followed by increasing polarisation and short-circuiting, was also observed in Na|Na-β″-alumina cells [27]. Other conclusions should not be transferred without testing. The larger Na^+ ion changes coordination preferences and hence polymer solvation; stability windows and interphase products differ; sodium metal has different mechanical and chemical properties from lithium; and sodium cells use different cathode chemistries. In the framework of Section 14, sodium systems therefore require their own gate evidence: lithium-based data can motivate hypotheses but cannot pass a gate for a sodium cell.

5. Electrode materials through the solid-state lens

5.1. Cathodes

Layered oxides remain the leading cathodes, but a solid electrolyte changes their limitations. In liquid cells, particle cracking exposes fresh surface to the electrolyte; in solid cells, cracking separates particles from the electrolyte and from one another, so that loss of ionic contact rather than surface reaction can dominate capacity fade. Interphase formation and chemomechanical contact loss have been demonstrated in Ni-rich oxide|thiophosphate composites [25], and the volume change of electrode materials is now used as a design parameter for mechanically optimised ASSBs [90]. Single-crystal Ni-rich particles avoid intergranular cracking but exhibit other degradation modes [91]. Coatings are essential with sulfide catholytes [63,79], whereas halide catholytes permit 4 V operation without coatings [9,65]. The cathode is also the main oxygen source in cell-level thermal runaway [55].

Polyanionic cathodes such as $LiFePO_4$ deliver less energy but operate near 3.4 V with very small volume change, which makes them the natural partner for polymer electrolytes with limited oxidative stability [3]. High-voltage spinel and lithium-rich layered cathodes have comparatively limited evidence in the literature reviewed here; their additional oxygen-redox and voltage-window demands make them challenging for any electrolyte, so they are treated as open opportunities rather than established options. Conversion cathodes such as sulfur introduce other interface problems (large volume changes, electronic insulation) that are beyond the scope of this review.

5.2. Anodes

Lithium metal is central to the energy-density argument for SSBs and is the most demanding electrode partner. During stripping, lithium must be supplied to the interface at least as fast as it is removed; otherwise voids form and accumulate, increasing the local current density and seeding filaments during subsequent plating. In Li|Li_6PS_5Cl|Li cells, the critical stripping current was 0.2 and 1.0 mA cm^{-2} at stack pressures of 3 and 7 MPa, respectively, well below the plating limit of 2.0 mA cm^{-2}, and lithium was transported to the interface by creep rather than by diffusion [27]. Filament initiation and propagation are distinct processes, governed respectively by subsurface pores and microcracks and by the fracture toughness of the ceramic, and lower stack pressure suppresses propagation [60]. Electronic leakage allows lithium to deposit inside LLZO or Li_3PS_4 but not inside LiPON [72], and recent work links dendrite growth to electrochemical corrosion of the electrolyte [92]. Anode-free and interlayer designs, such as a silver–carbon composite layer in sulfide cells, avoid the handling of thick lithium foil and have achieved high-energy, long-cycling cells [66].

Silicon is the most instructive counterexample to the notion that solid electrolytes must be thermodynamically stable. The interphase that forms on micro-silicon in contact with a sulfide electrolyte passivates and prevents continuous interphase growth; this enabled 99.9 wt% micro-silicon anodes that operated at current densities up to 5 mA cm^{-2}, at temperatures from −20 to 80 °C and at areal capacities above 11 mAh cm^{-2} in full cells [67]. Columnar silicon, carbon-stabilised Li–Si and other alloy anodes extend this approach [93–95]. The price is mechanical: the volume change must be accommodated by stack pressure or cell architecture. Lithium–indium and $Li_4Ti_5O_{12}$ anodes are frequently used as stable laboratory counter electrodes [30,79]; they are

Table 6
Electrode materials evaluated for solid-state cells. Potentials are nominal values vs Li^+/Li; volume changes are qualitative.

Electrode	≈ Potential (V)	Volume change	SSB-specific limitation	Most compatible SE partner (evidence)	Status	Key refs
Ni-rich layered oxide (NCM ≥ 80% Ni)	3.6–4.3	Moderate, anisotropic	Contact loss by chemo-mechanics; SE oxidation; O_2 release	Halide catholyte; coated, with sulfide	Advanced lab/pilot	[25,55,65,90]
NCM (≤ 60% Ni), $LiCoO_2$	3.6–4.3	Moderate	SE oxidation; coating chemistry	Sulfide + coating; halide	Advanced lab	[9,64,79]
$LiFePO_4$	≈ 3.4	Small	Low energy; low electronic conductivity	Polymer (PEO)	Commercial with polymers	[3]
High-voltage spinel / Li-rich layered	≥ 4.5 / oxygen redox	Moderate	Extreme oxidative demand	Evidence limited	Open	,
Lithium metal	0	Very large (plating/stripping)	Voids, filaments, electronic leakage, pressure window	Garnet with interlayer; argyrodite; polymer (warm)	Lab/pilot	[12,27,60,72]
Anode-free / Ag–C interlayer	0	Very large	Coulombic efficiency; interlayer stability	Sulfide	Demonstrated (lab/pouch)	[66]
Micro-silicon / alloys	≈ 0.1–0.5	Very large	Pressure needed; carbon promotes SE decomposition	Sulfide (passivating)	Advanced lab	[67,93–95]
Li–In, $Li_4Ti_5O_{12}$	≈ 0.6 / 1.55	Small–moderate	Low energy; masks anode problems	Sulfide	Laboratory reference only	[30,79]

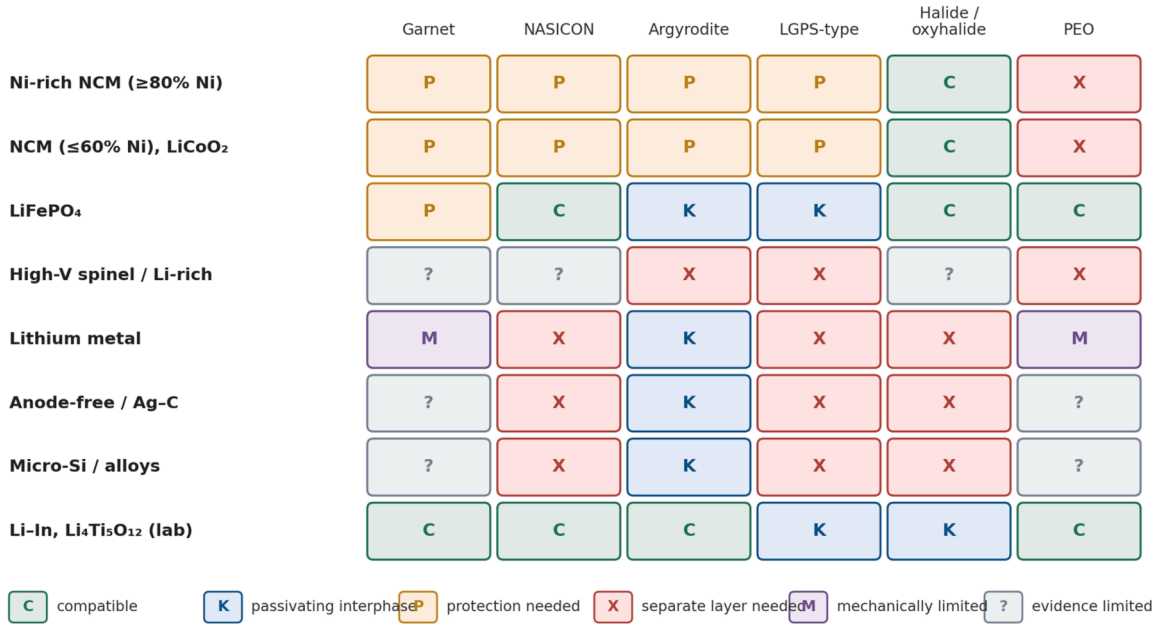


Fig. 5. Electrode–electrolyte compatibility matrix. Rows, electrodes; columns, electrolyte families. Each cell indicates the dominant compatibility mode: compatible (C), kinetically stabilised by a passivating interphase (K), protection or interlayer required (P), incompatible without a separate electrolyte layer (X), mechanically limited (M) or evidence limited (?). Expert synthesis based on refs [3,9,12,17,25,27,65–67,79].

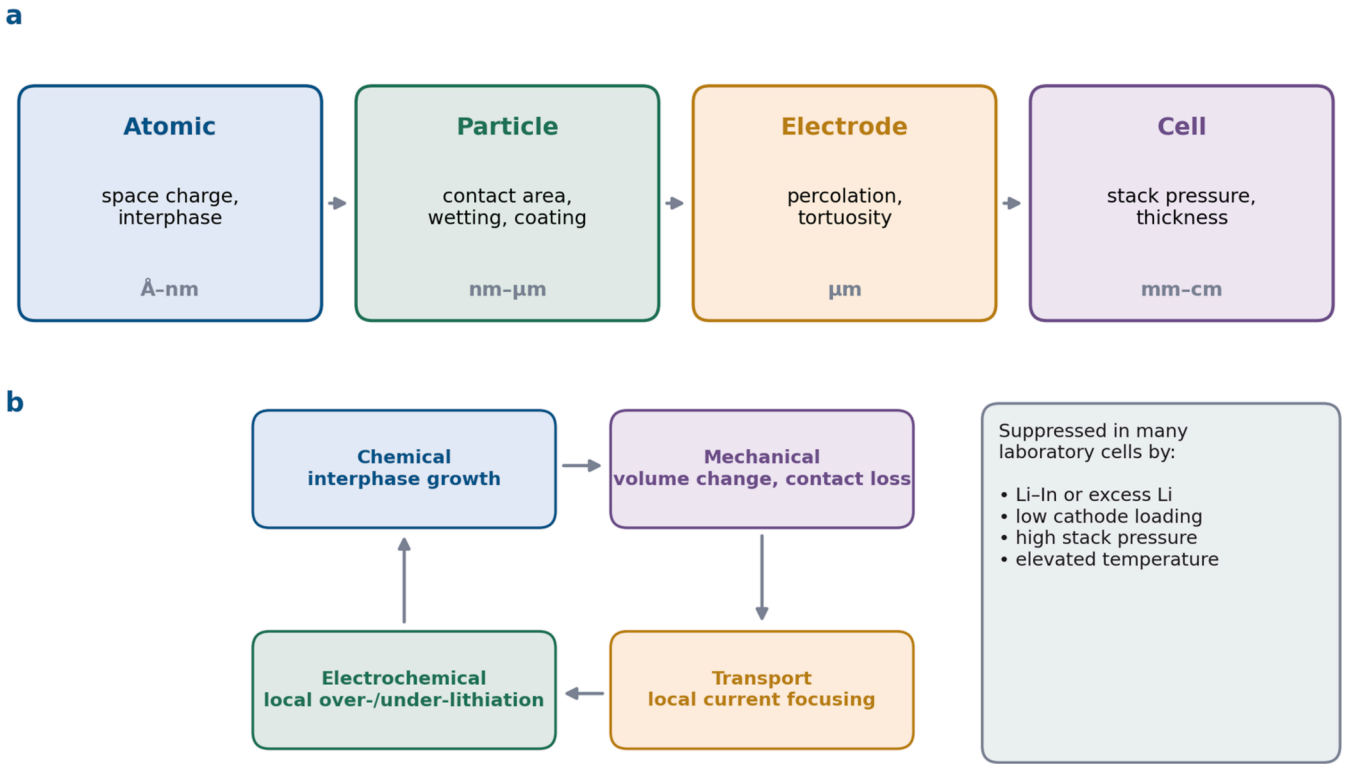


Fig. 6. The interface as a multiscale, coupled system. (a) Length scales at which the electrode–electrolyte interface is defined, from space charge and interphase (Å–nm) to particle contact (nm–µm), electrode percolation (µm) and cell-level pressure and thickness (mm–cm). (b) Coupled degradation: interphase growth changes volume and contact, contact loss concentrates current, and focused current accelerates local decomposition and filament initiation; common laboratory conditions that suppress this cascade are listed on the right. Based on refs [22–25,27,60].

convenient for studying cathode behaviour but conceal problems that would arise in a practical cell, and data obtained with them should not be extrapolated to lithium metal.

5.3. *Pairing principles*

Four criteria determine the compatibility of an electrode with an electrolyte at their interface: (a) the electrode potential relative to the

practical stability window of the electrolyte; (b) the nature of the interphase (electronically insulating and self-limiting or not); (c) the mechanical compatibility between the volume change of the electrode material and the compliance of the electrolyte; and (d) the microstructural compatibility of particle size and volume fraction in the composite electrode [96]. Table 6 and Fig. 5 apply these criteria. The best-performing combinations in the literature are not simply pairs of materials that satisfy all four criteria intrinsically; rather, they satisfy at least one criterion by design: a coating provides chemical compatibility, a catholyte provides oxidative stability, pressure maintains mechanical contact, and particle-size engineering provides percolation.

6. The electrode–electrolyte interface: formation, chemistry, electrochemistry, mechanics and transport

The interface in a solid-state cell is not a plane but a multiscale object (Fig. 6a). At the atomic scale it comprises space-charge regions and interphases a few nanometres thick; at the particle scale, the fraction of active-material surface in ionic contact with the electrolyte; at the electrode scale, the percolating network whose tortuosity sets the effective transport; and at the cell scale, the pressure-bearing interfaces between layers, whose thickness and flatness determine the current distribution. The processes at these scales are coupled and cannot be optimised independently (Fig. 6b).

6.1. How solid–solid interfaces form

Interface formation proceeds through four overlapping stages, each of which leaves a measurable signature. **Assembly contact.** Solid–solid contact is created mechanically by cold pressing (sulfides, halides), by sintering or co-sintering (oxides), by deposition (thin films, ALD layers) or by casting and in situ polymerisation (polymers) [11,12,85]. The initial contact area depends on particle size, surface roughness, fabrication pressure and the plasticity of both phases; the wide range of pressing pressures and durations used by different laboratories [30] is therefore a range of initial interfaces. Surface layers formed before assembly, carbonate and hydroxide on garnet [70] or residual carbonate on coated cathodes [79], become part of the interface. **Chemical reaction.** On contact, chemical-potential mismatch drives reaction where kinetics allow, and co-sintering can cause interdiffusion between oxide electrolytes and cathodes [11,76]. **Electrochemical decomposition.** During the first charge, the electrolyte is exposed to oxidising potentials at the cathode and reducing potentials at the anode; decomposition continues until the products either passivate (electronically insulating, ionically conducting) or keep growing (mixed conducting) [15,22,26,78]. Where the lithium chemical potential changes abruptly across the interface, space-charge layers may also form (Section 6.4). **Electro--chemo-mechanical evolution.** Cycling adds volume change, void formation at lithium anodes and crack formation in cathode particles, all of which reduce the contact established during assembly [24,25,27,60]. These stages explain why nominally identical materials yield different interfaces in different laboratories, and why interface quality must be reported together with processing history (Box 1).

6.2. Thermodynamic versus kinetic stability

Grand-potential phase diagrams based on DFT energies determine whether an electrolyte is thermodynamically stable at a given lithium chemical potential and which products form when it is not [14,22]. These calculations show that most fast conductors, in particular thiophosphates, are thermodynamically unstable at the potentials of both lithium-metal anodes and layered-oxide cathodes [15]. Yet many such electrolytes work in cells. The resolution is kinetic. The practical stability windows of argyrodite, garnet and NASICON electrolytes are considerably wider than those predicted for direct decomposition, because decomposition proceeds through intermediate lithiated and delithiated states of the electrolyte [26]. If the products are electronically insulating, the reaction is self-limiting; if they conduct electrons, it can continue. Examples are the micro-silicon anode stabilised by a passivating sulfide interphase [67] and the machine-learning analysis of AIMD interface simulations, which predicted that many electrolytes classified as unstable by thermodynamic screening would be stable or passivating against lithium [59]. Fig. 7 summarises this distinction. The design question therefore becomes whether the interphase is self-limiting, ionically conducting and electronically insulating under operating conditions, a kinetic question that thermodynamic screening alone cannot answer.

6.3. Interphases are not inert

A passivating interphase, the product of reaction between the electrode and the electrolyte, is far from a neutral spectator. Reversible and irreversible capacity can arise from (de)lithiation of the electrolyte-derived phases that mediate indirect decomposition [26], so part of the charge attributed to the cathode in early cycles may originate from the electrolyte. Carbon-free electrode designs improve interfacial stability partly because conductive carbon enlarges the electrolyte area exposed to electron transfer [67]. Even well-established cathode coatings are not fully designed: carbonate incorporated into sol–gel $LiNbO_3$ coatings alters their kinetics, and the benefit of a coating depends on the thiophosphate electrolyte used [79]. The function of a coating is thus a property of the coating and of both of its neighbours.

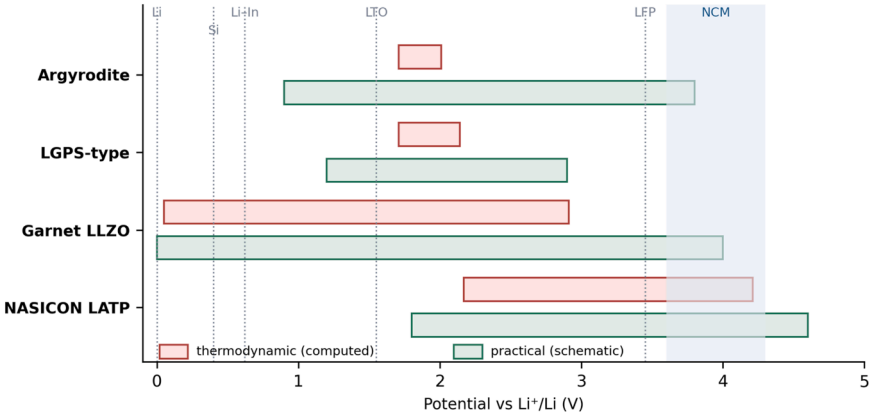


Fig. 7. Thermodynamic versus practical stability windows. The intrinsic (direct-decomposition) window of each electrolyte is compared with the practical window, which is widened by passivating interphases and by indirect decomposition through (de)lithiated electrolyte states; nominal electrode potentials are indicated. Window positions are schematic; refs [14,15,22,26] provide computed and measured values.

6.4. Space-charge layers: a contested contributor

Space-charge layers form wherever the lithium chemical potential changes abruptly at an ionic interface. First-principles calculations predicted lithium depletion at the oxide-cathode|sulfide interface and suggested that it could be a major source of interfacial resistance [97]. A continuum model of typical electrode–electrolyte combinations estimated that space-charge layers are usually thinner than a nanometre and contribute negligible resistance, except for lithium-depleted layers [98]. In contrast, two-dimensional exchange NMR across a $Li_xV_2O_5$|$Li_{1.5}Al_{0.5}Ge_{1.5}(PO_4)_3$ interface showed that formation of a space-charge layer raised the activation energy for interfacial lithium exchange from 0.315 to 0.515 eV [99]. The evidence is contradictory, and the contradiction is informative: space-charge effects appear significant under lithium depletion and at clean interfaces without interphases or coatings, whereas in practical composite electrodes they are difficult to separate from interphase and contact resistance. We therefore regard space charge as a contested contributor to high interfacial impedance rather than as a general explanation.

6.5. Chemo-mechanics and contact loss

Solid–solid contact can be maintained only mechanically. The volume of active materials changes with lithium content, the stiffness and creep resistance of electrolytes vary by orders of magnitude, and the resulting stresses open gaps and cracks [24,90]. Capacity fade in Ni-rich cathode composites results from both chemomechanical contact loss and interphase formation [25]. At the electrode scale, the particle-size distributions of active material and electrolyte determine whether ionic pathways percolate at high active-material loading; percolation is favoured when the electrolyte particles are smaller than the active-material particles [96]. These are not second-order effects: they decide whether the conductivity of the electrolyte is accessible at all.

6.6. Lithium-metal interfaces

Four mechanisms with direct experimental evidence limit lithium-metal interfaces. First, voids formed during stripping raise the local current density and seed filaments that grow during plating, so the stripping rate rather than the plating rate limits power [27]. Second, filament initiation proceeds by lithium filling subsurface pores connected by microcracks, and propagation proceeds by wedge opening, which depends on fracture toughness, filament length, current density, and stack pressure [60,100]. Third, electronic leakage allows lithium to accumulate inside the electrolyte away from the anode [72], as can local variations in electronic structure at grain boundaries [71,73]. Fourth, electrochemical corrosion of the electrolyte has been linked to dendrite growth [92], and garnets have been reported to have an intrinsic upper limit of critical current density [101]. None of these mechanisms is captured by the ionic conductivity or the thermodynamic stability of the electrolyte.

6.7. Why half-cell success does not translate to full cells

The coupling in Fig. 6b explains why. A small heterogeneity in interphase resistance or contact focuses current, causing local over- or under-lithiation, local volume change, further contact loss, and further current focusing. This cascade is suppressed in the configurations most commonly used to report new materials: indium or excess-lithium counter electrodes that buffer the anode, low cathode loading that shortens ionic pathways, high stack pressure that closes gaps, and elevated temperature that lowers kinetic barriers. Each of these is a valid means of isolating a mechanism, but each also removes a condition that a practical cell must tolerate. The inter-laboratory variability reported for an identical material set processed with different pressures, pressing times, and In-to-Li ratios [30] demonstrates the influence of such hidden variables. The same study identified an initial open-circuit voltage of 2.5–2.7 V vs Li^+/Li as a simple predictor of successful cycling for the materials used and recommended that results be reported in triplicate [30]. The mechanisms, their controlling variables, and their diagnostic signatures are collected in Table 7.

7. Interface engineering: mechanisms, limits and evidence

Interface-engineering strategies can be grouped by the mechanism they target (Fig. 8): chemical passivation, electronic insulation, mechanical compliance and contact, current homogenisation, and processing that sets thickness and density. Table 8 assesses each strategy by mechanism, advantage, limitation, scalability, validation-scale grade (A–D, defined in Table 3) and remaining challenge.

Cathode coatings. Coatings act as ionically conducting, electronically insulating barriers between an oxidizing cathode and an electrolyte that would otherwise decompose; an ideal coating is ionically conductive, electronically insulating, chemically compatible with both neighbors and conformal. In sulfide cells, the benefit of $LiNbO_3$-type coatings depends on their residual carbonate content and on the thiophosphate

Table 7
Electrode–electrolyte degradation mechanisms. Control: thermodynamic (T) or kinetic/mechanical (K).

Mechanism	Driving force	Control	Diagnostic signature	Most affected systems	Evidence	Key refs
Direct decomposition to stable products	Chemical-potential mismatch	T	Interphase phases (XPS, ToF-SIMS); impedance growth	Thiophosphates at cathode and anode	Strong (computation + experiment)	[14,22]
Indirect decomposition via (de)lithiated SE	Redox activity of SE	K	Extra capacity; reversible SE redox	Argyrodite, garnet, NASICON	Strong	[26]
Non-passivating (mixed-conducting) interphase	Electronic conduction of products	K	Continuous impedance rise	LGPS-type vs Li	Strong	[15,78]
Chemical interdiffusion during processing	Temperature + reactivity	T/K	Secondary phases after co-sintering	Garnet/oxide cathodes	Moderate	[11,76]
Space-charge depletion	Li chemical-potential step	T	Change in interfacial activation energy	Oxide cathode|sulfide; model interfaces	Contested	[97–99]
Contact loss from cathode volume change	Anisotropic lattice change	K	Capacity loss without interphase growth; voids in cross-sections	Ni-rich NCM composites	Strong	[25,90]
Void formation on Li stripping	Stripping flux > creep supply	K	Critical stripping current; pressure dependence	Li|sulfide, Li|garnet	Strong	[27]
Filament initiation / propagation	Pore pressure; wedge opening	K	Short circuit; tomography of cracks	Li|ceramic electrolytes	Strong	[60, 100]
Internal Li deposition	Electronic leakage; GB electronic states	K	Li inside the bulk (neutron depth profiling)	LLZO, Li_3PS_4	Strong	[72,73]
Moisture-derived surface layers	Reaction with air	K	Wetting failure; H_2S	Garnet; thiophosphates	Moderate	[3,70]

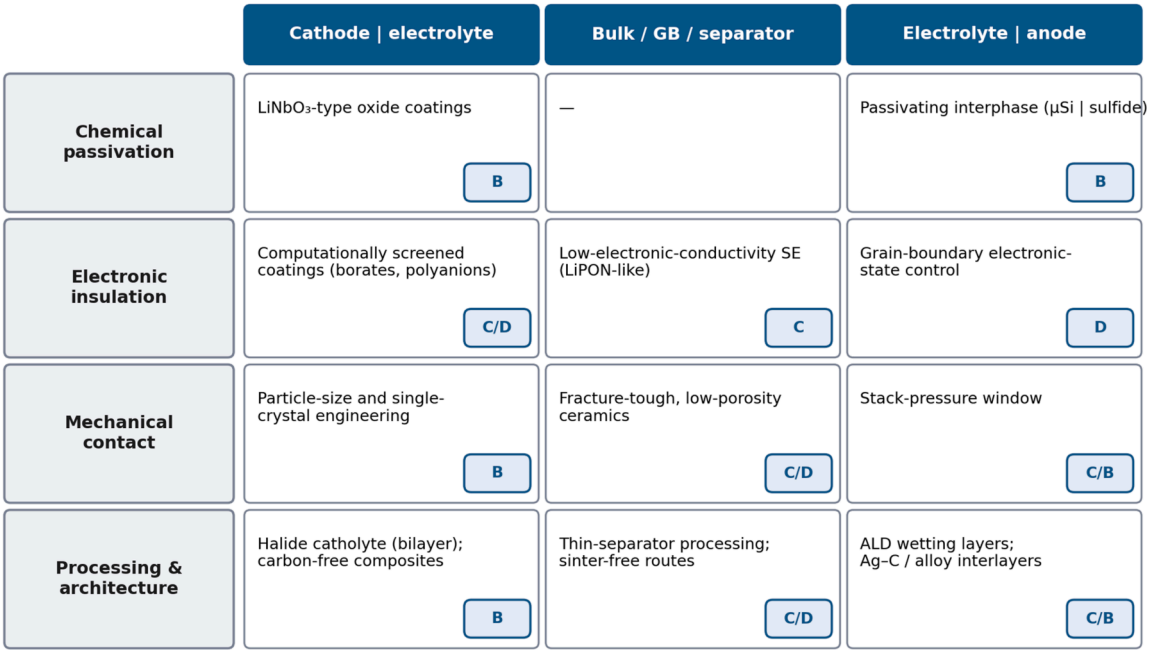


Fig. 8. Interface-engineering strategy map. Strategies are arranged by the interface on which they act (cathode|electrolyte; electrolyte bulk, grain boundary and separator; electrolyte|anode) and by the mechanism class they target. Badges give the validation-scale grade defined in Table 3. Based on refs [11,12,27,60,63,64,66,67,79,96].

Table 8
Interface-engineering strategies. Validation-scale grade (Table 3): A, full cells at practical loading in several groups; B, full cells under laboratory conditions; C, symmetric, half or model cells; D, computational or proposed.

Strategy	Mechanism	Advantage	Limitation	Scalability	Grade	Remaining challenge	Refs
Oxide coatings on cathodes ($LiNbO_3$-type)	Kinetic barrier; electronic insulation	Enables sulfide catholytes at 4 V	Composition- (carbonate) and thickness-sensitive; SE-dependent	Wet chemistry scalable	B	Mechanistic design rules; conformality at scale	[25,79]
Computationally screened coatings (polyanions, borates)	Chemical/electrochemical compatibility with both neighbours	Rational pre-selection	Few candidates validated; long-term behaviour unknown	Depends on chemistry	B/D	Validation beyond single cathode/SE pairs	[63,64]
Halide catholyte (bilayer)	Oxidatively stable SE at cathode	Uncoated 4 V operation	Adds halide|sulfide junction; reduction at anode	Cold pressing	B	Stability of internal junction	[9,65,81]
ALD wetting interlayers on garnet	Lithiophilic lithiated interphase	Removes assembly contact resistance	Does not address stripping voids or filaments	ALD cost / throughput	C/B	Durability at high current	[12]
Ag–C / alloy interlayers (anode-free)	Alloying; homogenised plating	No thick Li foil; high energy	Requires high Coulombic efficiency	Coating processes	B	Long-term evolution of interlayer	[66,95]
Passivating anode interphase (μSi + sulfide)	Self-limiting insulating interphase	No continuous SEI growth	Volume change needs pressure	Scalable powders	B	Low-pressure operation	[67,93,94]
Particle-size / single-crystal engineering	Percolation; crack suppression	High loading; less contact loss	Kinetics of large particles	Established powder routes	B	Co-optimisation with SE particle size	[91,96]
Stack-pressure control	Mechanical contact; creep supply	Raises stripping limit; reliable Li cycling at 5 MPa	Promotes propagation; system cost	Pack-level engineering	C/B	Defining safe pressure windows	[27,60,102]
Thin-separator ceramic processing	Density at low thickness	Cell-level energy density	Li loss; interdiffusion; brittleness	Unproven at scale	C/D	Large-area, defect-free films	[11,74,75]

electrolyte used [79]. Computational screening of coating candidates for phase, chemical and electrochemical stability and ionic conductivity identified polyanionic oxides and borates as promising coatings [63], and a combined computational and microscopy study confirmed that a predicted $Li_3B_{11}O_{18}$ coating outperforms Li_2ZrO_3 on NCM [64]. This is one of the clearest examples of interface design in which computation-guided selection was followed by experimental validation; notably, the validated criterion was chemical and electrochemical compatibility rather than bulk conductivity. Comparing these studies reveals a recurring pattern: a coating selected for stability performs well with one cathode–electrolyte pair, but its transfer to another electrolyte is not guaranteed [64,79], which is why coatings are graded B rather than A in Table 8.

Anode-side interlayers. For wetting, an ultrathin ALD Al_2O_3 layer reduced the Li|garnet interfacial resistance from 1710 to 1 Ω cm^2 [12]. Such layers solve the contact problem at assembly but do not, by themselves, prevent void formation during stripping or filament propagation, which are controlled by current density, pressure, and microstructure [27,60]. Anode-free sulfide cells have been realised with silver–carbon interlayers [66], and alloy anodes reduce the reactivity of lithium [95].

Microstructure and architecture. Particle-size engineering enables

Table 9
Characterisation techniques for solid-state interfaces, electrolytes and cells: measured quantities, supportable conclusions, limitations and complementary methods.

Technique	What it measures	Conclusions it can support	Limitations and artefacts	Complementary methods
EIS (equivalent circuit or DRT)	Bulk, grain-boundary and interfacial resistances; capacitances	Magnitude and evolution of ASR; separation of processes by time constant	Non-unique fits; arc assignment; pressure, contact and temperature dependence; per-interface vs total [103,105]	Thickness/temperature series; reference electrodes; XPS; microscopy
DC polarisation (blocking electrodes)	Electronic conductivity	Risk of internal Li deposition	Contact quality; polarisation time; very small currents [72]	Neutron depth profiling; microscopy
Transference number (Bruce–Vincent; Hittorf)	Cation transference	Concentration polarisation in polymers	Method-dependent; interfacial-resistance changes [86,87]	Modelling; NMR (with caution)
Transmission-line EIS of composites	Ionic resistance in porous electrodes; tortuosity	Composite transport limitation	Assumes negligible electronic resistance and uniform reaction [106]	Tomography; FIB-SEM
CCD test (2- or 3-electrode)	Current at short circuit or divergent polarisation	Plating vs stripping limits	Step size, capacity per step, pressure, T; 2-electrode tests conflate plating and stripping [27]	Cross-sections; operando imaging
Galvanostatic cycling (symmetric, half, full)	Capacity, efficiency, polarisation, retention	Cell-level performance	Li–In or excess Li hides anode problems; replicates needed [30]	EIS during cycling; post-mortem
XRD (incl. operando)	Crystalline phases; lattice parameters	Bulk phase changes; strain	Insensitive to thin or amorphous interphases; automated phase ID can mislead [36]	XPS; NMR; TEM
XPS / ToF-SIMS (in situ or ex situ)	Interphase chemistry; depth profiles	Identity of decomposition products	Transfer reactions; beam and sputter damage; surface-limited [78]	EIS; TEM; NMR
Raman / FTIR	Local bonding; polymer–salt coordination; ion association	Solvation structure; degradation products	Fluorescence; weak signals from thin layers [21]	NMR; DFT/MD
Solid-state NMR (incl. 2D exchange)	Local Li dynamics; interfacial exchange	Transport across interfaces; space-charge effects	Model systems; signal assignment [99]	EIS; simulation
Neutron depth profiling	Li concentration profiles	Internal Li deposition	Facility access; depth resolution [72]	DC polarisation; microscopy
SEM/FIB/TEM (cryo or inert transfer)	Morphology; voids; cracks; coatings	Contact loss; coating degradation	Local; beam and air sensitivity [25,27,64]	Tomography; EIS
X-ray tomography / operando imaging	3D microstructure; crack and filament growth	Failure mechanism and location	Resolution vs field of view; special cells [60]	Electrochemistry in the same cell
DSC / TGA	T_g, crystallinity, residual solvent; T_{onset} and ΔH of mixtures	Thermal stability of materials and mixtures	Heating rate, SOC, sealing, mass ratio; not cell-level [52,53]	ARC; gas analysis
ARC and abuse tests (thermal ramp, short circuit, nail)	Self-heating, trigger and maximum temperatures; gas release	Cell-level safety	Format- and SOC-dependent; few SSB datasets [4,55]	Thermal modelling [57,68]
Mechanical and pressure-dependent tests	Modulus, hardness, fracture toughness; pressure–performance relations	Gate 2 parameters; pressure windows	Pressure must be monitored during cycling [102]	Chemo-mechanical models

high active-material loading without loss of percolation; single-crystal cathodes reduce intergranular cracking; carbon-free electrodes reduce parasitic electrolyte decomposition; and catholyte/separator/anolyte multilayers assign each electrolyte to the interface it can tolerate.

Pressure: a double-edged parameter. Increasing stack pressure raised the critical stripping current in Li|argyrodite cells [27], whereas lower stack pressure reduced the tendency of filaments to propagate once initiated [60]. Reliable lithium plating and stripping for >1000 h in symmetric cells, and >200 cycles in Li|Li_6PS_5Cl|$LiNi_{0.80}Co_{0.15}Al_{0.05}O_2$ full cells at room temperature, were obtained at a comparatively low stack pressure of 5 MPa [102], and low operating pressure reduced the apparent ionic conductivity through poorer electrolyte–current-collector contact without necessarily harming cyclability [103]. These results indicate that a pressure window, rather than a maximum pressure, should be specified. Pressure is therefore not a free parameter to be maximised: pressures above those that an economically viable pack can provide shift cost from the material to the system [29,104].

Processing. From a ceramic-processing standpoint, the separator problem is to achieve near-theoretical density at the thickness of polymer separators without lithium loss or interdiffusion [11]. Low-temperature film deposition, sinter-free routes and co-designed all-ceramic cathode composites address part of this problem [74–76]. Pressure- and field-assisted densification routes are proposed as promising for achieving high density at a relatively low thermal budget but, in our view, they have not yet been proven at relevant scale for thin, large-area separators or for co-sintered cathode layers.

8. Experimental techniques for interfaces, electrolytes and cell performance

Interface claims are only as reliable as the measurements behind them. This section summarises what the main techniques measure, which conclusions they can support and where they can mislead (Table 9). A recurring principle is that no single technique proves an interfacial mechanism: electrochemical signatures must be correlated with chemical, structural and morphological evidence obtained under comparable conditions.

8.1. Electrochemical methods

Electrochemical impedance spectroscopy (EIS) separates processes by their relaxation times and is the main tool for measuring bulk, grain-boundary and interfacial resistances [105]. Its limitations are frequently underestimated. Equivalent-circuit fits are not unique, and similar spectra can arise from different physical models; assigning an arc to grain boundaries or to an interface requires analysis of capacitances, variation of thickness, temperature or electrode type and, ideally, a reference electrode [105]. Distribution-of-relaxation-times analysis reduces some ambiguities but depends on regularisation choices that should be reported. Spectra also depend on stack pressure, temperature and the contact between electrolyte and current collector: low operating pressure reduced the apparent conductivity of sulfide electrolytes through poorer contact [103], and identical samples measured in different laboratories differed by up to 4.5 mS cm^{-1} [31]. Whether an ASR refers to one interface or to both interfaces of a symmetric cell must

be stated, because this choice alone produces a factor-of-two difference.

DC polarisation with ion-blocking electrodes measures the electronic conductivity that controls internal lithium deposition [72]. With non-blocking electrodes, DC polarisation combined with EIS (the Bruce–Vincent method) estimates transference numbers [86], subject to the limitations discussed in Section 4.4 [87]. Transmission-line analysis of impedance spectra of symmetric cells separates the ionic resistance within porous electrodes from the charge-transfer resistance [106] and underpins the composite-electrode estimates in Section 9.1.

Critical current density (CCD) tests increase the current stepwise until short circuit or divergent polarisation. The result depends on step size, areal capacity per step, temperature, pressure and whether plating and stripping are separated: three-electrode measurements showed that the critical stripping current (0.2–1.0 mA cm^{-2}, depending on pressure) can lie far below the plating limit (2.0 mA cm^{-2}) [27]. A CCD value reported without these conditions cannot be compared with other values.

Galvanostatic cycling, rate capability and cell configuration. Symmetric Li|SE|Li cells probe the anode interface, half-cells with Li–In counter electrodes probe the cathode composite, and full cells probe the interaction of both; only full cells reveal crosstalk and the current-focusing cascade of Section 6.7 [30,79]. Capacity retention should be reported together with areal loading, N/P ratio, C-rate, temperature, stack pressure and the number of replicate cells [30].

8.2. Structural and chemical characterisation

X-ray diffraction (XRD) identifies crystalline phases and lattice changes but is insensitive to thin or amorphous interphases, and automated phase identification can be misleading, as critiques of autonomous synthesis have shown [36]. **X-ray photoelectron spectroscopy (XPS)** and time-of-flight secondary-ion mass spectrometry (ToF-SIMS) identify interphase chemistry; in situ XPS during lithium deposition has directly revealed the decomposition products of LGPS upon lithium exposure [78], whereas ex situ samples can react during transfer, and sputter depth profiling can reduce or alter species. **Raman and infrared spectroscopy** probe local bonding, polymer–salt coordination, and ion association in polymer electrolytes [18,21]. **Solid-state NMR**, including two-dimensional exchange experiments, quantifies local lithium dynamics and interfacial exchange, as in the space-charge study discussed in Section 6.4 [99]. **Neutron depth profiling** detects lithium deposited inside the bulk electrolyte [72].

8.3. Microscopy and tomography

Scanning electron microscopy with energy-dispersive spectroscopy, focused-ion-beam cross-sections and transmission electron microscopy reveal contact loss, voids, cracks and coating degradation [25,27,64]. Cryogenic or inert-transfer protocols are required for lithium and sulfides, which are sensitive to the electron beam and to air. X-ray tomography and operando imaging connect microstructure with failure; filament initiation and propagation were resolved in this way [60]. Because microscopy is local, statistically representative sampling is needed before observations are generalised to an electrode.

8.4. Thermal, mechanical and safety testing

DSC and thermogravimetric analysis characterise crystallinity, glass transition and residual solvent in polymers, as well as the onset temperature and heat release of SE–electrode mixtures [52,53]; the results depend on heating rate, sample mass, state of charge and crucible sealing, which must be reported [53]. Accelerating-rate calorimetry (ARC) on complete cells yields the characteristic temperatures of self-heating, triggering and maximum temperature used for liquid-electrolyte cells [4], and should be applied to solid-state cells at representative states of charge [55]. Mechanical tests (nanoindentation, compression, fracture toughness) and pressure-controlled cycling fixtures quantify the parameters of Gate 2 (Section 14); the stack pressure should be monitored during cycling rather than only set at assembly [102].

8.5. Operando and in situ methods

Operando EIS, XPS, Raman, NMR, XRD and imaging track the evolution of interfaces under current [60,78,105]. Their main limitation is the compromise in cell geometry, pressure and beam exposure required for access, which can make the observed interface unrepresentative of a practical cell. Operando data are most informative when the same cell configuration is also cycled under standard conditions.

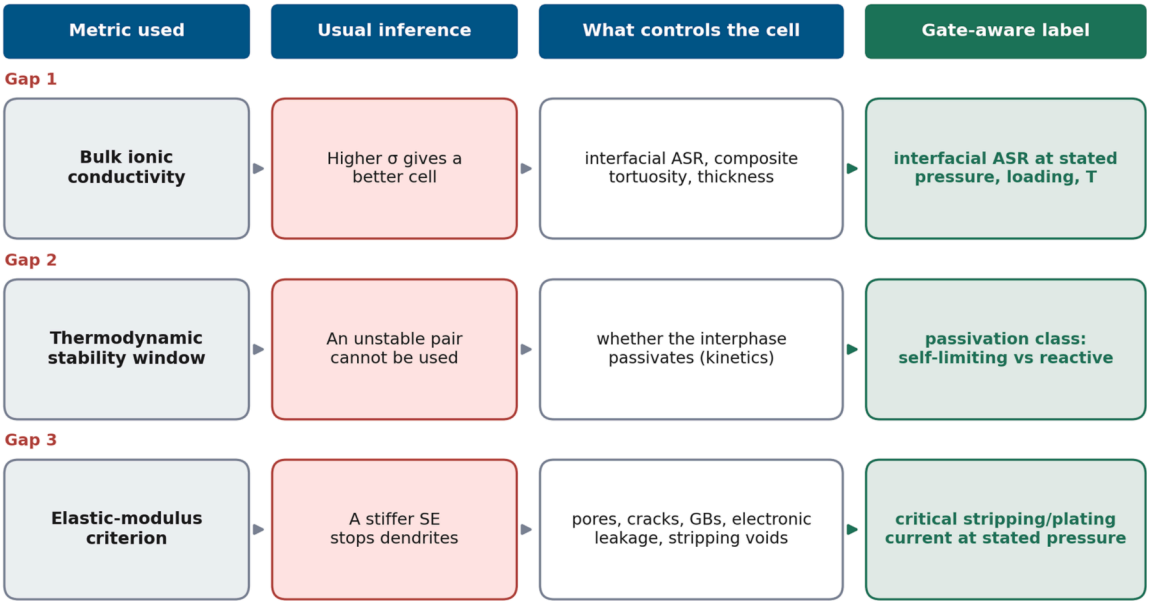


Fig. 9. Three translation gaps. For each commonly used metric, the inference usually drawn, the processes that actually control cell behaviour and a proposed gate-aware label closer to the cell-level failure mode. Based on refs [12,26,31,58–61,67,72,100,107].

Table 10
Area-specific resistance budget at j = 3 mA cm^{-2}. 'Reported' values are taken from the cited source; 'derived' values are calculated with Eqs. (1)–(3) from the stated inputs. Conductivities of 1–10 mS cm^{-1} span the range reported for sulfide electrolytes [6,7,31]; ε/τ = 0.03–0.15 corresponds to ε ≈ 0.3 and τ ≈ 2–10 and is illustrative.

Component	Relation	Inputs (source)	ASR (Ω cm^2)	ΔV at 3 mA cm^{-2}	Status
Separator	Eq. (1)	L = 30 μm; σ = 10 mS cm^{-1}	0.3	0.9 mV	Derived
Separator	Eq. (1)	L = 30 μm; σ = 1 mS cm^{-1}	3	9 mV	Derived
Laboratory pellet	Eq. (1)	L = 500 μm; σ = 1 mS cm^{-1}	50	150 mV	Derived
Li|garnet, as assembled	Measured	LLCZN, room temperature [12]	1710	5.13 V (cell inoperable)	ASR reported; ΔV derived
Li|garnet, ALD-Al_2O_3	Measured	Room temperature [12]	1	3 mV	ASR reported; ΔV derived
Composite cathode	Eq. (3)	L_{el} = 100 μm; σ = 10 mS cm^{-1}; ε/τ = 0.15	2.2	6.7 mV	Derived
Composite cathode	Eq. (3)	L_{el} = 100 μm; σ = 10 mS cm^{-1}; ε/τ = 0.03	11.1	33 mV	Derived
Composite cathode	Eq. (3)	L_{el} = 100 μm; σ = 1 mS cm^{-1}; ε/τ = 0.15	22.2	67 mV	Derived
Composite cathode	Eq. (3)	L_{el} = 100 μm; σ = 1 mS cm^{-1}; ε/τ = 0.03	111	333 mV	Derived
Total ohmic budget	Eq. (2)	ΔV_{allow} = 0.1 V; j = 3 mA cm^{-2}	≤ 33	100 mV	Proposed design target

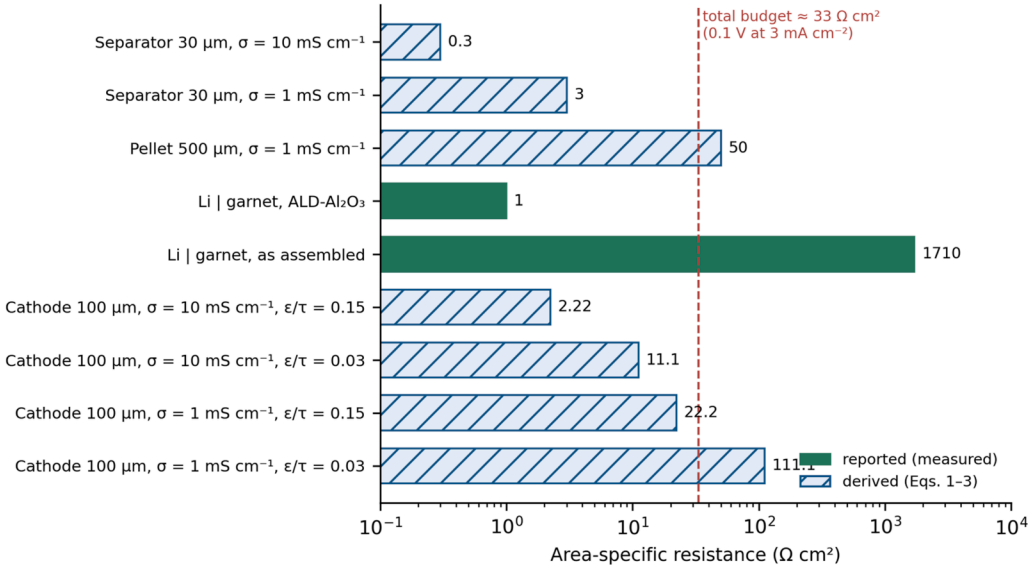


Fig. 10. Area-specific resistance budget for representative cell components (logarithmic scale). Solid bars: Li|garnet interfacial resistances reported at room temperature in ref [12]. Hatched bars: values derived with Eqs. (1)–(3) for illustrative thicknesses, conductivities and ε/τ ratios (Table 10). The dashed line marks a proposed total ohmic budget of 33 Ω cm^2 (0.1 V at 3 mA cm^{-2}). Values obtained in different configurations are compared only by order of magnitude.

8.6. Comparability rules adopted in this review

From this assessment we adopt four rules that are applied throughout the remainder of the review: (i) conductivities or resistances are compared only when temperature, pressure, thickness and electrode type are known; (ii) differences smaller than the documented inter-laboratory spread are not interpreted [31]; (iii) a mechanism is accepted only when electrochemical and chemical or morphological evidence agree; and (iv) results obtained with Li–In or excess-lithium configurations are not extrapolated to lithium-metal full cells [30].

9. Three translation gaps: where bulk metrics and descriptors mislead

The preceding sections reveal a common problem in experimental and computational research: three quantities commonly used to compare solid electrolytes fail, in identifiable situations, to predict cell behaviour (Fig. 9). The same quantities are among the most frequently used targets and filters in ML studies, so these gaps transfer directly into AI-driven discovery.

9.1. Gap 1: conductivity is not cell impedance, a quantitative resistance budget

To compare bulk, interfacial and composite-electrode contributions on a common basis, we express each as an area-specific resistance (ASR, Ω cm^2) and as the ohmic voltage drop ΔV at a current density j:

$$ASR_{sep} = L_{sep} / \sigma_{SE}. \quad (1)$$

$$\Delta V = j \times ASR. \quad (2)$$

where L_{sep} is the separator thickness and σ_{SE} the electrolyte conductivity. For a composite electrode of thickness L_{el} in which the electrolyte occupies a volume fraction ε with tortuosity factor τ, the effective ionic conductivity is $\sigma_{eff} = \sigma_{SE}\ \varepsilon/\tau$. In the transmission-line limit with negligible electronic resistance and a uniform reaction distribution, the ionic contribution of the electrode to the d.c. resistance is approximately one-third-of its through-thickness ionic resistance [106]:

$$ASR_{el,ion} \approx L_{el} / (3\ \sigma_{SE}\ \varepsilon/\tau). \quad (3)$$

Eq. (3) underestimates the loss when ionic transport limits the reaction distribution and should therefore be regarded as a lower bound. Table 10 and Fig. 10 apply Eqs. (1)–(3) at a reference current density of 3 mA cm^{-2}, which corresponds approximately to a 1C rate for a 3 mAh cm^{-2} electrode. All calculated values were checked independently; reported (measured) and derived values are distinguished.

Three conclusions follow. First, a 30 μm separator contributes 0.3–3 Ω cm^2 (0.9–9 mV) for σ between 10 and 1 mS cm^{-1}, whereas the thick pellets (≈500 μm) common in laboratory tests contribute ~50 Ω cm^2 at 1 mS cm^{-1}; pellet cells therefore overstate the importance of separator

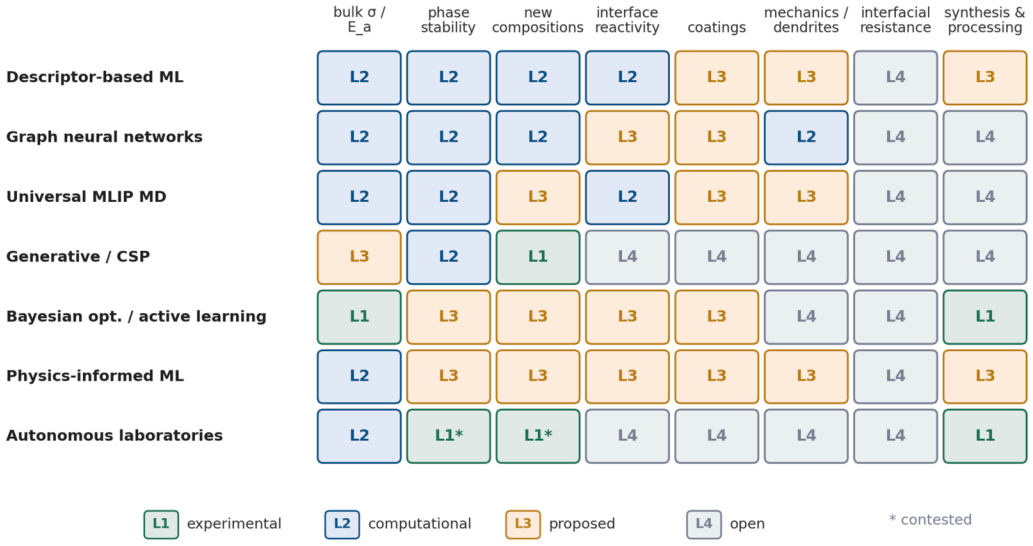


Fig. 11. Evidence map for AI in solid-state battery research. Rows, AI method classes; columns, target properties from bulk conductivity to interfacial resistance and processing. Each cell shows the highest evidence level identified in this review (L1, experimentally demonstrated; L2, computationally demonstrated; L3, conceptually proposed; L4, open opportunity); an asterisk marks a contested L1 claim. Grades are consistent with Tables 11 and 12.

resistance in practical cells. Second, measured interfacial resistances span more than three orders of magnitude for a single materials pair: the as-assembled Li|garnet interface (1710 Ω cm^2) would correspond to a 5.1 V drop at 3 mA cm^{-2}, that is, the cell could not operate, whereas the ALD-treated interface (1 Ω cm^2) contributes 3 mV [12]. Third, with illustrative composite parameters, the ionic resistance of a 100 μm composite electrode is 22–111 Ω cm^2 for $\sigma_{SE} = 1$ mS cm^{-1} and 2.2–11 Ω cm^2 for $\sigma_{SE} = 10$ mS cm^{-1}, because only 3–15% of the bulk conductivity is accessible. Thus, once a separator material exceeds ~1 mS cm^{-1} and can be made thin, further gains in bulk conductivity benefit mainly the composite electrode, where they remain valuable for thick electrodes [58], while the interface determines whether the cell works at all. A total ohmic budget of 0.1 V at 3 mA cm^{-2}, which we propose as a design target rather than an established threshold, corresponds to $ASR_{total} \leq 33$ Ω cm^2; the as-assembled garnet interface exceeds it by a factor of ~50, and the low-ε/τ composite at 1 mS cm^{-1} exceeds it on its own.

These estimates have explicit limitations. They neglect charge-transfer and solid-state diffusion resistances in the active particles, the electronic resistance of the composite, concentration polarisation (important for polymer electrolytes with low transference numbers, Section 4.4) and the temperature and pressure dependence of all terms. The measured values come from different cell configurations and are combined only to compare orders of magnitude. Finally, conductivities of the same material can differ between laboratories by up to 4.5 mS cm^{-1} (a factor of ≈4.5 between the lowest and highest values for the most conductive sample) [31], so literature values within this range should not be ranked.

Table 11
AI techniques for electrolyte and electrode discovery, graded by evidence level (L1–L4) and validation-scale grade (A–D) as defined in Table 3.

Method	Target	Data (size)	Validation	Level / grade	Key limitation	Refs
DFT descriptors + neural network	Fast-ion conduction	DFT-derived, small	Computational	L2/D	Descriptor transferability	[109]
Multi-descriptor logistic regression	Conductivity class	Experimental literature (small)	Later DFT-MD	L2/D	No single descriptor predictive; label noise	[110,111]
Transfer learning	Conductivity	Small experimental set	Computational	L2/D	Domain shift	[112]
Curated database + composition classifier	Conductivity class	820 entries; 403 RT compositions	Retrospective	L2/D	No microstructure/ processing metadata	[113]
GNN-predicted moduli + deposition criteria	Dendrite suppression	> 12,000 solids	Computational	L2/D	Criterion validity (Gap 3)	[107]
Scaled GNN stability prediction	Phase stability; zero-shot σ	2.2 million predicted stable	736 independently realised	L2/D	Novelty/utility debated	[32,37, 114]
Universal MLIP molecular dynamics	E_a, σ	Pre-trained; near-equilibrium-biased	vs DFT	L2/D	Softening; ~150 meV E_a underestimate	[38,62, 115,116]
AI + HPC screening pipeline	Stability + σ	> 32 million → 18	Synthesis + conductivity	L1/C	Validated within a known family	[33]
Unsupervised phase-field selection + CSP	New phases	Reported crystalline materials	Synthesis	L1/C	Discovery efficiency ≠ property optimisation	[117]
Bayesian optimisation of synthesis	Process → σ	Sequential experiments	Measured σ > 7 mS cm^{-1}	L1/C	Low-dimensional; mechanism post hoc	[34]
Arrhenius-informed MPNN (polymers)	σ(T)	Hundreds of publications	Computational/ retrospective	L2/D	Literature heterogeneity	[88]
Autonomous BO (polymer formulations)	σ	Closed loop	Measured	L1/C (provisional)	Preprint; not yet peer reviewed	[89]
Deep learning of cathode electrochemistry	Voltage/capacity	Experimental (liquid cells)	Retrospective	L2/D	Transfer to SSB untested	[118]
Autonomous synthesis laboratory	Synthesis of predicted phases	Robotic	Contested novelty	L1 (contested)/ C	Automated phase identification; disorder	[35,36]

9.2. Gap 2: thermodynamic windows are not practical stability

Thermodynamic screening correctly predicts that most fast conductors are unstable at electrode potentials [14,15], but it cannot predict whether the interphase will passivate. Indirect decomposition widens practical windows [26], passivating sulfide interphases enable silicon anodes [67], and an AIMD-trained classifier predicted that hundreds of electrolytes classified as unstable by the convex-hull criterion would be stable or passivating against lithium [59]. The converse holds for garnets: although close to thermodynamic stability against lithium, they fail through poor wetting, voids and electronic leakage [12,72]. Stability windows are therefore only a weak label for whether an interface will work.

9.3. Gap 3: elastic-modulus criteria are not dendrite resistance

Linear stability analysis showed that interfacial roughening at a lithium|polymer interface is suppressed when the shear modulus of the separator is roughly twice that of lithium, for Poisson's ratios similar to that of PEO [61], and generalised criteria were developed for anisotropic solid–solid interfaces [108]. >12,000 inorganic solids were screened against these criteria using elastic moduli predicted by graph neural networks (GNNs) [107]. Yet ceramics far stiffer than lithium are penetrated through flaws, subsurface pores and electronically active grain boundaries [60,71–73,100]. Modulus-based criteria describe the roughening of an ideal interface, whereas practical failure is dominated by defects, fracture and electronic leakage.

9.4. Implication: label validity

If a target label falls into one of these gaps, a model can be accurate yet irrelevant. We therefore recommend that AI studies in this field report, alongside their accuracy metrics, which cell-level failure mode their label is intended to represent and what evidence links the two. Gate-aware labels include the passivation class of an interface (rather than its reaction energy), the stripping-limited critical current at a specified pressure, and the interfacial ASR under stated conditions.

10. AI for electrolytes and electrodes: an evidence-graded assessment

Fig. 11 maps AI method classes against target properties; the colour of each cell indicates the highest evidence level found, and details are given in Table 11. Level 1 evidence is concentrated on bulk phases, compositions and synthesis parameters, whereas interface targets remain at Levels 2–4. Grades are reported in the combined notation of Section 2.5 (evidence level/validation-scale grade).

10.1. Descriptor-based learning from small experimental datasets

Early efforts screened fast lithium conductors with DFT-derived descriptors and neural networks [109]. In a holistic screening of >12,000 candidates, a logistic-regression model trained on experimental literature data, combined with electronic-conductivity, cost and stability filters, reduced the candidate list to 21 promising materials [110]. Two findings of that study remain relevant: no single descriptor was predictive, and the multi-descriptor model had only a useful degree of predictive power. Subsequent studies assessed ML-proposed candidates with DFT molecular dynamics [111], and transfer learning was proposed specifically for small experimental datasets [112]. The size of the data problem is quantified by an expert-curated database of experimentally measured conductivities containing 820 entries from 214 sources and 403 unique compositions measured near room temperature, which its authors used to train a classifier that helps experimentalists prioritise candidates [113]. We grade these methods as Level 2 (L2/D): they are useful for prioritisation, but few of their predictions have been tested prospectively by synthesis.

10.2. Large-scale structure prediction and universal interatomic potentials

Graph networks trained on large DFT datasets predicted 2.2 million structures below the known convex hull, 736 of which had been independently realised in experiments, and the resulting potential was used for zero-shot predictions of ionic conductivity [32]. Generative models now propose inorganic structures directly [119]. To be relevant to SSBs, these capabilities must meet two requirements. First, accurate formation energies do not guarantee accurate stability predictions, especially in sparse chemical spaces [114], and the meaning of discovery at this scale has been questioned [37]. Second, the universal machine-learning interatomic potentials (uMLIPs) that make large-scale transport simulations affordable [115,116] systematically soften the potential-energy surface and underestimate Li^+ migration barriers [38]; a high-throughput study reported that a universal potential underestimated Li^+ activation energies by ~150 meV relative to DFT [62]. At a fixed prefactor, an error of this size corresponds to a ~340-fold overestimate of room-temperature conductivity ($\exp[0.150\ \mathrm{eV}/(k_B \times 298\ \mathrm{K})] \approx 344$), which would populate a screening list with false positives. The softening is systematic and can be reduced by fine-tuning [38], and a recent preprint argues that current uMLIPs are adequate for solid ion conductors [120]. We consider uMLIPs suitable for pre-screening and for relative ranking within structurally similar families, provided that representative structures are checked with DFT or AIMD, but conductivity predictions from uncorrected universal potentials should not be presented as evidence for a new compound.

10.3. Experimentally validated discovery and optimisation

Level 1 evidence exists and is informative. Unsupervised learning of element combinations in reported phase fields, combined with crystal-structure prediction, prioritised the synthesis of a new quaternary lithium solid electrolyte [117], and related computation-guided searches established new sulfide phases [121]. A cloud-scale pipeline combining AI models and physics-based methods screened >32 million candidates, predicted roughly half a million potentially stable materials, and synthesised and characterised compositions of $Na_xLi_{3-x}YCl_6$ within about 80 h [33]. Because the validated compositions belong to a known halide family [9], the demonstration tests the pipeline rather than chemical novelty (L1/C). Several target compounds were synthesised on an autonomous platform [35], but a subsequent analysis concluded that none of the claimed new materials was truly new, owing to uncertain automated Rietveld analysis and neglect of compositional disorder in the predictions [36]; we therefore record this case as a contested Level 1 claim.

The strongest Level 1 examples in the electrolyte literature are low-dimensional process optimisations with direct measurement. Gaussian-process-based Bayesian optimisation of the solid-state synthesis of tetragonal Li_7SiPS_8 was reported to achieve conductivities above 7 mS cm^{-1}, up to 350% higher than the previous synthesis route, while lowering the synthesis temperature by 100 K and shortening the reaction time by 76 h [34] (L1/C). The lesson is that AI currently performs best in small design spaces, with fast and directly relevant measurements and closed feedback loops.

10.4. Polymer electrolytes

The experimental literature on polymer electrolytes is comparatively large. A message-passing neural network whose readout layer was constrained to the Arrhenius equation, trained on conductivity data from hundreds of publications, predicted the conductivities of several thousand candidate formulations and was more accurate than a model without explicit temperature dependence [88]. This is an example of physics-informed learning in which domain knowledge compensates for

Table 12
AI for interface problems, graded by evidence level and validation-scale grade (Table 3).

Interface problem	AI approach	Data	Prediction	Validation	Level / grade	Main limitation	Refs
SE|Li reactivity and passivation	Classifier on AIMD-derived labels	67 interfaces (50/17)	Stable / passivating / reactive	AIMD; 35.3% validation error	L2/D	Tiny computational dataset; no experiment	[59]
Cathode coating selection	DFT tiered screening (ML extension proposed)	DFT database	Stable, conducting coatings	Borate coating confirmed experimentally	DFT-guided (non-ML) case validated at C/B; ML extension L3/D	ML extension untested	[63, 64]
Interface structure and ion transport	MLIP molecular dynamics	DFT/AIMD training	Interfacial diffusion, reactions	vs DFT	L2/D	Reactive configurations under-sampled; softening	[38, 41, 42]
Dendrite/deposition stability	GNN moduli + analytical criteria	> 12,000 solids	Stability class	Computational	L2/D	Criterion misses flaws and electronic leakage	[61, 107]
Critical current, voids, filaments	,	No suitable dataset identified	,	,	L4	Data absent	[27, 60]
Interfacial resistance and space charge	,	No curated dataset identified	,	,	L4	Metadata absent; contested physics	[31, 98, 99]
Interface processing (coating thickness, sintering, pressure)	Bayesian optimisation (proposed)	Sequential experiments	Process window	Demonstrated for bulk synthesis only	L3/D	Multi-objective; slow cell tests	[30, 34]

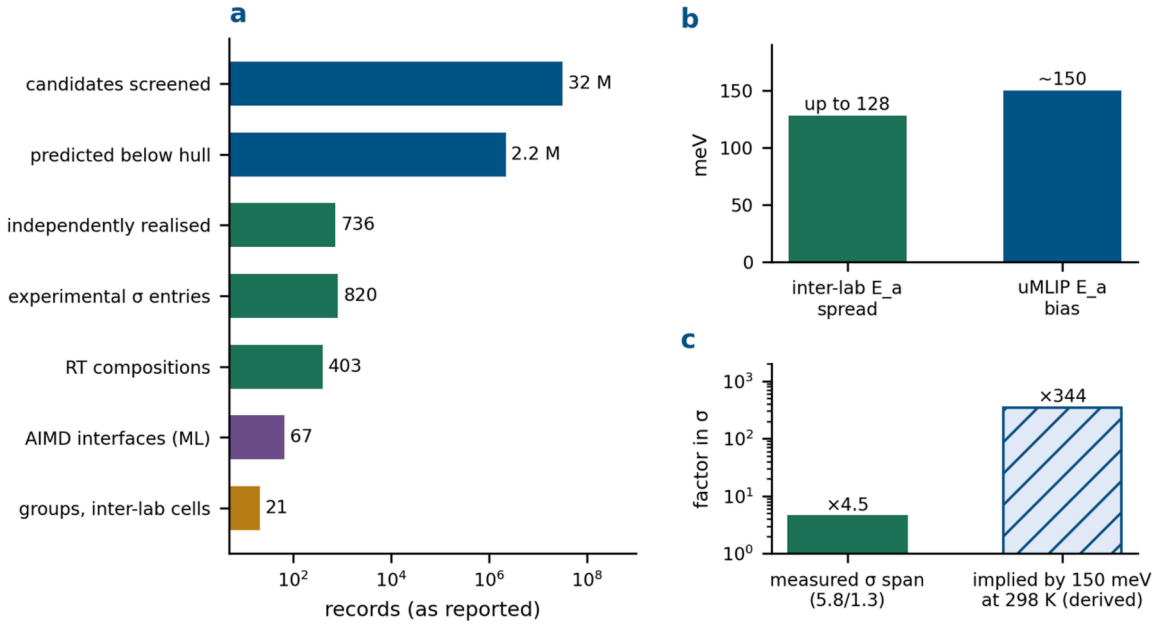


Fig. 12. Data asymmetry and the experimental noise floor. (a) Number of records reported at successive levels of the data hierarchy, from screened and predicted structures to experimentally characterised interfaces and inter-laboratory cell studies (logarithmic scale; the categories are not equivalent units and are shown only to compare orders of magnitude) [30,32,33,59,113]. (b) Inter-laboratory spread of activation energies measured for identical argyrodite samples [31] compared with the systematic activation-energy underestimate of a universal potential [62]. (c) The same quantities expressed as conductivity factors: the measured span for the most conductive sample (5.8/1.3 mS cm^{-1}) [31] and the factor implied by a 150 meV bias at 298 K (derived).

limited data (L2/D). A closed-loop Bayesian-optimisation campaign on an autonomous platform identified, within about a month, poly(ε-caprolactone)-based formulations with conductivities comparable to the best PEO electrolytes [89]; because this result is reported in a preprint, we record it as a provisional Level 1 claim (L1/C, provisional). Recent reviews of sodium polymer electrolytes identify AI and ML as a future direction for solvation-structure design rather than as an established route [21].

10.5. Electrodes

Deep learning of experimental electrochemistry across many cathode compositions has been demonstrated [118], and AI for electrode materials has been reviewed more broadly [44]. However, we found few models for solid-state electrodes trained on solid-state data. This matters because the dominant failure modes differ: surface reaction and cracking in liquid cells, contact loss in solid cells (Section 5.1). We therefore grade electrode AI for SSBs as Level 3 for degradation and Level 4 for joint electrode–electrolyte optimisation.

11. AI for the electrode–electrolyte interface

The interface is where AI is most needed and least effective. The evidence is summarised in Table 12.

Reactivity and passivation. The most direct attempt to learn interfacial behaviour trained classifiers on AIMD simulations of 67 electrolyte|Li interfaces to predict, from structural features, whether an interface is stable, passivating or reactive [59]. Conceptually, this

replaces a thermodynamic label with a kinetic one. Its limitations are also instructive: because AIMD is expensive, the model was trained on 50 interfaces and tested on 17, with a validation misclassification rate of 35.3% (6 of 17), and the highlighted candidates were checked by further AIMD rather than by experiment [59]. This is good Level 2 work (L2/D) and a clear illustration of how small interface datasets currently are.

Coatings. The tiered DFT screening of coating materials [63] and the subsequent experimental confirmation of a borate coating [64] could be extended by ML to multicomponent and amorphous coatings; to our knowledge, this has not yet been demonstrated experimentally (L3/D).

Interatomic potentials at interfaces. Machine-learned potentials allow simulations of interfaces containing thousands of atoms over nanosecond time scales and have been applied to electrolyte interfaces [41,42]. Two cautions apply. The near-equilibrium datasets used to train universal potentials under-represent reactive interface configurations, so active learning or fine-tuning is required for interfaces [38]. In addition, simulated time scales remain far shorter than the hours-to-months range over which interphases grow in cells.

Mechanics, filaments and critical current. Screening based on ML-predicted elastic properties [107] is Level 2 and shares the criterion problem of Gap 3. We found no AI model validated against experimental critical current densities, filament initiation or stripping-void formation (Level 4).

Interfacial resistance, space charge, adhesion and pressure response. We could not find a curated public dataset of experimentally measured interfacial resistance with the metadata required for learning (processing history, pressure, temperature, loading, impedance-fitting method), nor a validated AI model of these quantities (Level 4). This is the most critical gap in the field, because these quantities are among the main determinants of cell impedance (Section 9.1).

Table 13
Challenges for AI applied to solid-state battery interfaces.

Challenge	Consequence for models	Evidence	Mitigation
Scarcity of interface labels	Models restricted to bulk or computational proxies	403 RT compositions; 67 AIMD interfaces; no curated interfacial-resistance set [59,113]	Community datasets using the MIDR (Box 1); multi-fidelity learning
Label noise (inter-laboratory)	Error floor; spurious rankings	RSD 35–50% for σ; 21-group cell variability [30,31]	Report replicates and uncertainty; round-robin reference materials
Method bias in computed labels	Systematic false positives	~150 meV E_a underestimate; PES softening [38,62]	Fine-tuning; DFT/AIMD spot checks; bias correction
Missing processing/ microstructure metadata	Composition-only models cannot learn GB or contact effects	[30,113]	Mandatory fields for density, grain size, pressure, temperature
Near-duplicate families	Leakage; inflated accuracy	Family-dominated datasets [113]	Grouped splits; out-of-distribution tests
Weak labels (translation gaps)	Accurate but irrelevant predictions	Section 9 [59,60,107]	Gate-aware labels tied to failure modes
Publication bias (few negative results)	Poorly calibrated classifiers	Literature-derived training sets [110,113]	Publish negative and failed syntheses with metadata
Uncalibrated uncertainty	Over-confident screening	[38,114]	Uncertainty-aware models; Bayesian optimisation and active learning [34]
Retrospective-only validation	Optimistic performance estimates	[45,46]	Report prospective tests separately; use reporting checklists

12. The data problem: can AI predict interfaces from limited, heterogeneous data?

This question can be addressed quantitatively, because the relevant datasets have been counted and the relevant measurement uncertainties have been measured (Fig. 12).

Data asymmetry. Computed structures number in the millions [32] and are stored in open repositories such as the Materials Project [122], and a single screening pipeline can process tens of millions of candidates [33]. A comprehensive experimental dataset of lithium-ion conductivities contains 403 unique compositions near room temperature [113]. The largest ML study of interface reactivity was trained on 67 AIMD simulations [59], and the most systematic inter-laboratory study of full-cell performance evaluated one material set in 21 groups [30]. We found no curated public dataset of experimentally measured interfacial resistance, critical current density or interphase growth. The available data therefore shrink by orders of magnitude from bulk structures to the interfacial quantities that dominate cell behaviour (Section 9.1).

The noise floor. For identical materials, activation energies measured in different laboratories differed by up to 128 meV [31], and processing pressures, pressing durations and anode compositions also varied widely between groups in full-cell tests [30]. These spreads define a noise floor: a model trained on pooled literature values cannot be meaningfully assessed below this range, and reported errors smaller than the inter-laboratory spread suggest that the model is learning laboratory artefacts or that information is leaking between the training and test sets. The ~150 meV activation-energy underestimate of a universal potential [62] is a method bias that exceeds the experimental inter-laboratory range (Fig. 12b); expressed as a conductivity factor at 298 K, it corresponds to ~340-fold, compared with a ≈ 4.5-fold span between the lowest and highest conductivities measured for one sample (Fig. 12c) [31].

Heterogeneity and missing metadata. Reported 'total' conductivity combines bulk and grain-boundary contributions that depend on density, grain size and synthesis route as well as on composition, and most literature records do not report these variables [113]. Interfacial resistances depend in addition on stack pressure, temperature, loading, coating chemistry and the impedance-fitting choice, which are also reported inconsistently.

Leakage and generalisation. Solid-electrolyte datasets are dominated by families of closely related compositions (doped variants of a few parent structures). Random train–test splits therefore place near-duplicates on both sides and overestimate performance; family-wise or cluster-wise splits and explicit out-of-distribution tests are needed. The broader materials-ML literature shows why this matters: formation-energy accuracy did not translate into accurate stability predictions [114], standardised benchmarks were needed to compare methods fairly [123], reporting checklists have been proposed to make ML studies reproducible and open to critical assessment [45,46], and universal potentials perform poorly on average for configurations far from equilibrium [38].

Physics as a data multiplier. Where data are scarce, physically constrained models perform better. Encoding Arrhenius behaviour in the readout of a network improved polymer-electrolyte predictions [88]; physically meaningful structural descriptors can be derived from anion-framework topology [124] and from corner-sharing frameworks [125]; and transfer learning from large computational datasets can partly compensate for small experimental datasets [112].

Answer. With current data, AI can rank bulk-property candidates within known chemistries, optimise low-dimensional synthesis and processing when each suggestion is measured directly, and classify interface reactivity from computational labels with moderate accuracy.

Table 14
Complementary methods for interface research and how they are best coupled.

Method	What it provides	Typical scale	Blind spots	Best coupled with
DFT (grand-potential phase diagrams)	Reaction energies, decomposition products, windows	Static; unit cells	Kinetics, passivation, mechanics	AIMD/MLIP for kinetics [14,22]
AIMD	Early interfacial reaction pathways	~10^2 atoms; ~10^1–10^2 ps	Time and length scale; cost limits datasets	ML classifiers trained on AIMD [59]
Machine-learned interatomic potentials	Large, long interface simulations; transport	~10^3–10^5 atoms; ns	Training-set coverage; PES softening	Active learning; DFT spot checks [38,41]
Continuum electrochemical and thermal models	Polarisation, current distribution, heat release	μm–cm; s–h	Need measured parameters; simplified interface physics	Transmission-line EIS; calorimetry [57,68,106]
Chemo-mechanical, fracture and phase-field models	Stress, contact loss, crack and filament growth	nm–mm	Scarce constitutive data for interfaces	Tomography; pressure-dependent cycling [24,60,90]
Statistical ML / GNN	Fast screening across chemistries	10^5–10^7 candidates	Label validity; extrapolation	Physics constraints; uncertainty [88,114]
Bayesian optimisation / active learning	Efficient experiment selection	10^1–10^2 experiments	Low-dimensional; slow tests	Autonomous platforms [34]
Experiment (synthesis, impedance, operando)	Ground truth under operating conditions	Cell level	Noise, metadata gaps, throughput	MIDR; inter-laboratory references [30,31]

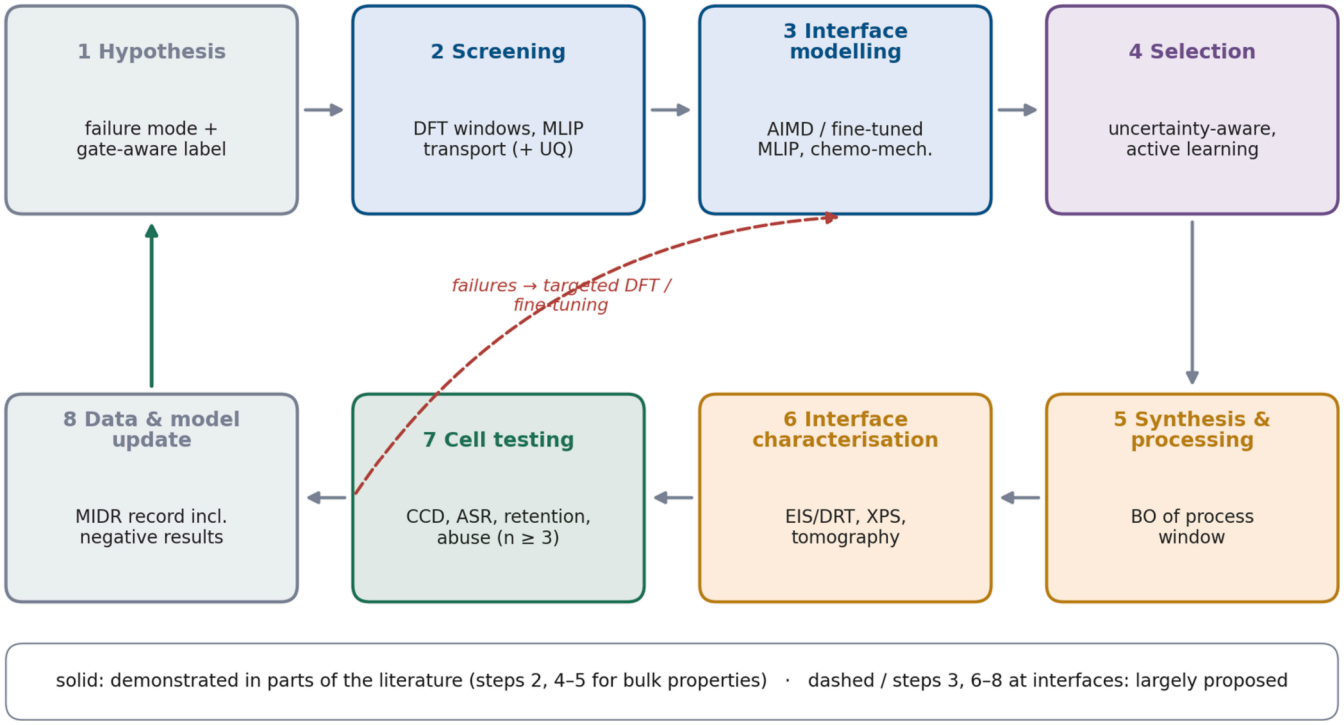


Fig. 13. Integrated theory–computation–experiment workflow for AI-assisted interface design. Steps 1–8 connect hypothesis generation, screening with uncertainty flags, interface modelling, uncertainty-aware selection, synthesis and processing optimisation, standardised interface characterisation, replicated cell tests and model updating with the Minimum Interface Data Record (Box 1). The dashed path returns failures for targeted DFT calculations or potential fine-tuning. Steps demonstrated in the literature for bulk properties are distinguished from interface-specific steps that remain largely proposed. Based on refs [30,31,33,34,38,59,63,64].

It cannot yet reliably predict experimentally measured interfacial resistance, critical current density or long-term interphase evolution, because these data are scarce and difficult to measure with low uncertainty. Data infrastructure, not algorithms, is the binding constraint. The main challenges and mitigations are summarised in Table 13, and a minimum reporting standard is proposed in Box 1.

Box 1 | Minimum Interface Data Record (MIDR): a proposed reporting standard. We propose that data reported for an electrode–electrolyte interface include at least: (1) identity: compositions of the electrolyte and of each electrode, including verified stoichiometry, synthesis route and phase purity; (2) microstructure: relative density, grain and particle-size distributions, electrolyte volume fraction in composites, and coating composition and thickness; (3) geometry: separator thickness, electrode areal loading, and anode excess or N/P ratio; (4) boundary conditions: fabrication pressure and duration, cycling stack pressure and temperature; (5) protocol: current densities, voltage window and formation procedure; (6) impedance method: cell configuration, reference electrode (if any), equivalent circuit or distribution-of-relaxation-times method, fitting uncertainty, and whether ASR values refer to one or two interfaces; (7) interphase characterisation: techniques and conditions; (8) failure: mode and cycle or time at failure; (9) uncertainty: number of replicate cells and their spread; (10) availability: raw data and negative results; and (11) for AI-derived predictions: the evidence level, the validation-scale grade and the gate addressed (Table 3, Section 14). Items (1)–(6) and (9) include the variables identified by inter-laboratory studies as major contributors to irreproducibility [30,31].

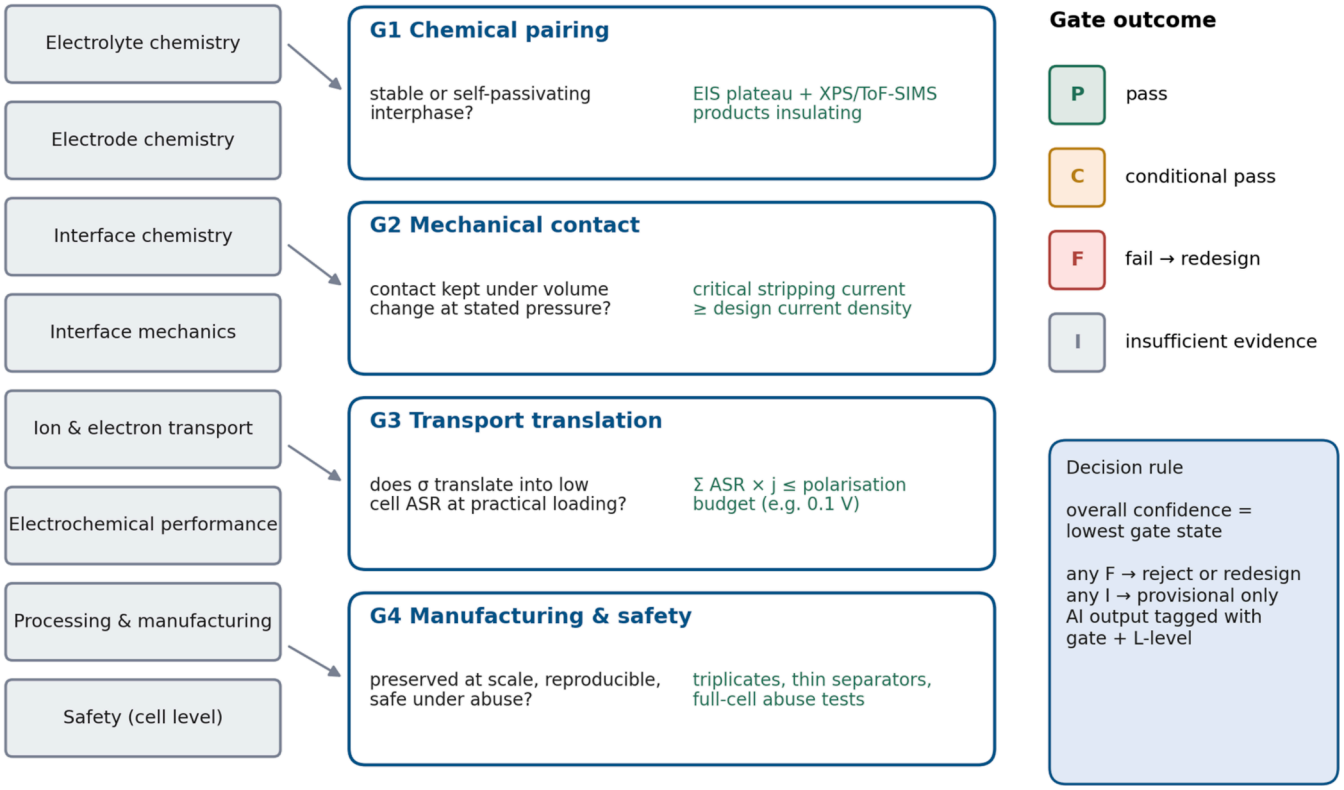


Fig. 14. Interface Co-Design Framework. Eight design layers are connected through four validity gates: G1, chemical pairing; G2, mechanical contact; G3, transport translation; and G4, manufacturing and safety validation. Each gate has a test question and an operational criterion (Table 15); gate outcomes are pass (P), conditional pass (C), fail (F) or insufficient evidence (I), and the overall confidence in a design equals the lowest gate outcome. AI predictions and experimental validation feed all gates and are labelled with the gate they address and their evidence level. Concept proposed in this review; evidence as in Tables 7, 8, 11, 12 and 15.

13. Integrating theory, DFT, machine-learning potentials, machine learning, continuum modelling and experimental design

No single method spans the length and time scales of an interface (Table 14). DFT provides reaction energies and electronic structure but not reaction kinetics at relevant scales; AIMD captures initial reaction kinetics on picosecond time scales for a few hundred atoms but cannot reach larger systems or longer times; machine-learned potentials extend simulations to larger systems and longer times but inherit the biases of their training data; statistical ML generalises across chemistries but requires reliable labels; and experiments provide ground truth under conditions that computations rarely reproduce. The key is to pair methods so that each covers the blind spots of the others.

Continuum and mesoscale models bridge atomistic simulations and cells. Thermodynamic and electrochemical models, grand-potential phase diagrams [14,22], porous-electrode and transmission-line models [106] and cell-level thermal models of failure scenarios [57,68], translate material properties into polarisation, heat release and stability. Chemo-mechanical, fracture and phase-field models link volume change, contact pressure and crack growth to contact loss and filament propagation [24,60,90], and linear-stability analyses underlie the modulus criteria discussed in Section 9.3 [61,108]. These models are most useful when they predict a quantity that can be measured in the same cell, such as an ASR, a critical current or a heat-release curve.

Translating predictions into decisions. Predictions become useful only when they are translated into specific synthesis, characterisation and cell-testing decisions. We propose four rules. (i) Each prediction should be stated as a falsifiable hypothesis about a gate-aware label, for example, that a coating keeps the cathode-interface ASR below a stated value after a stated number of cycles at a stated temperature and pressure, rather than about a bulk property. (ii) Uncertainty must be propagated: candidates whose predicted advantage is smaller than the method bias (e.g., ~150 meV for uncorrected uMLIP activation energies [62]) or the experimental noise floor [31] should not be prioritised over known reference materials. (iii) Experimental design should be sequential and uncertainty-aware: Bayesian optimisation and active learning select the next experiment where the expected information gain is highest, as demonstrated for low-dimensional synthesis problems [34,89]. (iv) Every experiment, including failures, should be reported with the metadata of Box 1 and fed back to retrain or recalibrate the models [45].

Fig. 13 presents a closed-loop workflow for interfaces in which uncertainty is propagated forward and information, with its metadata, is fed back. Parts of this workflow have been demonstrated for bulk properties: large-scale screening followed by synthesis [33], computation-guided coating selection followed by microscopy [63,64], and closed-loop optimisation of synthesis with measured conductivity [34]. The interface-specific steps, fine-tuned MLIP simulations of reactive interfaces, standardised interface characterisation and cell-level feedback into the models, remain largely proposed; to our knowledge, no published study has closed the full loop from interface prediction to validated cell-level performance.

14. An interface co-design framework with four validity gates

The analysis above suggests that sequential design, identifying the best conductor first, then compatible electrodes, and finally repairing the interface, is structurally suboptimal: each step optimises a quantity that may lie in a translation gap, and the problems postponed to later

Table 15
Operational criteria for the four validity gates. Anchor values are measured values from the cited studies under the stated conditions; screening targets are proposals of this review and must be adapted to the chemistry, format and application.

Gate	Test question	Required evidence and conditions	Pass / conditional / fail indicators	Anchor values (measured)	Proposed screening target	AI status
G1 Chemical pairing	Stable or self-passivating interphase under operating potentials?	DFT reaction energetics; time-resolved EIS; XPS/ToF-SIMS of products; stated T, potential window, cycles	P: ASR plateaus during formation, insulating products. C: requires coating/ catholyte. F: continuous growth or mixed-conducting products	LGPS|Li mixed-conducting growth [15,78]; passivating μSi|sulfide [67]	Interfacial ASR change approaches zero after formation; no universal value (baseline is chemistry-specific)	L2 [59]
G2 Mechanical contact	Contact kept under volume change and Li plating/stripping at stated pressure?	3-electrode critical stripping and plating currents; contact retention (EIS, cross-sections); stated pressure, T, capacity per step	P: critical stripping current ≥ design j at pack-feasible pressure. C: only at higher pressure or T. F: short or divergent polarisation below design j	0.2/1.0 mA cm^{-2} stripping at 3/7 MPa; 2.0 mA cm^{-2} plating [27]; >1000 h symmetric and >200 full-cell cycles at 5 MPa [102]	Critical stripping current ≥ design j (e.g., 3 mA cm^{-2}) with margin, at the pressure the application can supply	L2 (moduli); L4 (CCD, contact)
G3 Transport translation	Does σ translate into low cell ASR at practical loading?	Separator, interfacial and composite ASRs; electronic leakage; stated thickness, loading, T, pressure, fitting method	P: Σ ASR × j within budget. C: only at elevated T or low loading. F: budget exceeded at design conditions	Li|garnet 1710 → 1 Ω cm^2 [12]; derived budget (Table 10)	Report T_{onset}, ΔH, T_{max} and gas composition (Table 16)	L3–L4
G4 Manufacturing & safety	Preserved at scale, reproducible and safe under abuse?	Thin-layer processing; n ≥ 3 replicates; full-cell abuse tests at representative SOC; processing environment	P: reproducible within reported spread; no fire in full-cell abuse tests. C: needs dry room, inert processing or special packaging. F: runaway or unacceptable gas release	OCV 2.5–2.7 V vs Li^+/Li predicts cycling; triplicates [30]; crystalline sulfides stable vs lattice O_2 at 200 °C, react at 300 °C [53]; short-circuited ASSB can exceed Li-ion temperatures [57]		L1 (synthesis BO [34]); L3 (cell processing)

steps are often those that limit the cell. We therefore propose a co-design framework in which eight design layers (electrolyte chemistry, electrode chemistry, interface chemistry, interface mechanics, ion and electron transport, electrochemical performance, processing and manufacturing, and cell-level safety) are connected through four validity gates (Fig. 14). AI prediction and experimental validation are treated as evidence streams that feed every gate rather than as separate layers. A candidate cell design advances only if it passes the gate associated with each failure mode that limits its target metric, and every AI prediction is labelled with the gate to which it refers.

Operational definition of gate outcomes. Each gate is evaluated with four possible outcomes (Table 15). **Pass (P):** the required evidence exists at validation-scale grade B or better under conditions relevant to the target cell and meets the stated criterion. **Conditional pass (C):** the criterion is met only with a specified countermeasure (e.g., a coating, a catholyte or a minimum stack pressure) or within a restricted operating window, which then becomes a design constraint. **Fail (F):** the evidence shows that the criterion is not met under relevant conditions. **Insufficient evidence (I):** the evidence is only computational or proposed (grade D), was obtained in configurations that suppress the relevant failure mode (Section 6.7), or lacks the conditions required for comparison. The overall confidence in a design recommendation equals the lowest gate outcome: any F requires redesign, and any I limits the recommendation to 'provisional'. Numerical criteria are expressed either as literature anchor values measured under stated conditions or as proposed screening targets; the latter are design assumptions to be justified for each application, not universal thresholds.

Gate 1, chemical pairing. Does the electrode–electrolyte pair remain stable, or does it form a self-limiting, electronically insulating interphase during operation? Required evidence: reaction energetics together with kinetic evidence of passivation, time-resolved impedance showing that the interfacial resistance stabilises, and chemical identification of insulating products by XPS or ToF-SIMS [22,26,59,78], rather than thermodynamic windows alone. Failure is indicated by continuous resistance growth or by mixed-conducting products, as for LGPS against lithium [15,78]. AI status: reactivity classification is Level 2 [59]; the DFT-guided coating case is computation-guided rather than ML-based and was validated experimentally [63,64].

Gate 2, mechanical contact. Is ionic contact maintained at the intended stack pressure during electrode volume change and lithium plating and stripping? Required evidence: contact retention (impedance growth and cross-sectional void analysis) and separately measured critical stripping and plating currents at stated pressure and temperature [25,27,60]. Anchor values: critical stripping currents of 0.2 and 1.0 mA cm^{-2} at 3 and 7 MPa, compared with 2.0 mA cm^{-2} for plating, in Li|Li_6PS_5Cl cells [27]; stable cycling at 5 MPa in symmetric and full cells [102]. A design current density of 3 mA cm^{-2} (1C at 3 mAh cm^{-2}) exceeds the critical stripping current measured at 7 MPa by a factor of three, which illustrates why lithium-metal designs at practical rates currently receive at best a conditional pass. AI status: elastic properties, Level 2; contact evolution and critical currents, Level 4.

Gate 3, transport translation. Does bulk conductivity translate into low cell impedance at practical separator thickness and electrode loading? Required evidence: separator, interfacial and composite-electrode ASRs measured at realistic loading, and the electronic leakage of the electrolyte [12,58,72,96,106]. Proposed criterion: the sum of the ASRs multiplied by the design current density remains within the ohmic polarisation budget, for example, ≤33 Ω cm^2 for 0.1 V at 3 mA cm^{-2} (Section 9.1). AI status: Levels 3–4.

Gate 4, manufacturing and safety validation. Are the design properties preserved at practical thickness and area, in the processing environment, at a pack-feasible pressure, with acceptable reproducibility and under abuse? Required evidence: thin-layer processing, inter-batch or inter-laboratory reproducibility reported for at least three cells [30], and full-cell abuse tests with the metrics of Table 16 [11,30,53,55,57]. AI status: Level 1 for low-dimensional synthesis optimisation [34];

Table 16
Quantitative safety and operational metrics, measurement conditions and literature anchors. 'Status' distinguishes established measurements from proposed reporting criteria.

Metric	Definition / method	Conditions that must be reported	Anchor evidence (measured or modelled)	Status
Exothermic onset temperature and heat release (T_{onset}, ΔH)	DSC of SE + charged electrode mixtures	Heating rate, mass ratio, SOC, crucible sealing	Crystalline sulfides stable vs lattice O_2 at 200 °C, solid–solid reactions at 300 °C [53]; exotherms in ASSB microcells [52]	Measured; material level
Self-heating, trigger and maximum temperatures (T_1, T_2, T_3)	ARC on complete cells	Cell format, capacity, SOC, stack pressure	Definitions established for Li-ion [4]; O_2-induced runaway in Ah-level pouch cells [55]	Established method; SSB data scarce
Short-circuit temperature rise	Thermodynamic/thermal models; internal-short or nail tests	Energy content, liquid fraction, format	Short-circuited ASSB can exceed Li-ion temperatures [57]; large-format modelling [68]	Modelled
Pressure-dependent thermal behaviour	DSC/ARC on composites pressed at different pressures	Fabrication and operating pressure	Thermal-runaway behaviour of NCM811|Li_6PS_5Cl composites depends on pressure [69]	Emerging
Gas evolution	Gas analysis during heating or air exposure	Humidity, temperature, SOC	H_2S on hydrolysis [3]; oxygen-driven gas–solid pathways [53]	Measured
Interfacial ASR and its growth rate	EIS (3-electrode or symmetric), fitting method disclosed	T, pressure, cycle number, per-interface basis	1710 → 1 Ω cm^2 (Li|garnet) [12]	Measured; G1/G3 criterion
Critical stripping / plating current	Stepwise galvanostatic test, 3-electrode	Pressure, T, capacity per step	0.2/1.0 mA cm^{-2} (3/7 MPa) vs 2.0 mA cm^{-2} [27]	Measured; G2 criterion
Stack-pressure window	Pressure-controlled cycling with monitoring	Fabrication, contact and cycling pressure	Reliable Li cycling at 5 MPa [102]; lower pressure suppresses propagation [60]	Measured; chemistry-specific
Capacity retention / degradation rate	Galvanostatic full-cell cycling	Loading, N/P ratio, C-rate, T, pressure, replicates	>200 cycles at RT for Li|Li_6PS_5Cl|NCA at 5 MPa [102]; inter-laboratory variability [30]	Measured; no universal threshold
Reproducibility / failure probability	Fraction of cells meeting specification; OCV screening	$n \geq 3$; assembly protocol	OCV 2.5–2.7 V predictor; triplicate reporting [30]	Proposed reporting criterion

Level 3 for cell-level processing.

Quantitative safety and operational criteria. Table 16 lists the metrics that make the safety assessment and Gates 2–4 measurable, the conditions under which each must be measured, and literature anchor values where reliable values exist. Two limitations apply. First, most SSB-specific safety data come from powder mixtures, pellets or single-layer cells, and comparable full-cell thermal-runaway parameters, for example, the characteristic temperatures obtained by accelerating-rate calorimetry, remain scarce [4,53,55]. Second, thresholds depend on chemistry, format and application; we therefore present anchor values and reporting requirements rather than universal pass/fail limits.

Worked example 1: Ni-rich NCM | argyrodite | micro-silicon. G1: the uncoated cathode interface fails, so G1 at the cathode is a conditional pass that requires a coating [25,79]; at the anode, the sulfide interphase passivates [67] (pass). G2 is marginal at both electrodes: Ni-rich particles lose contact through anisotropic volume change [25], and silicon expansion must be accommodated by pressure [67] (conditional pass). G3 depends critically on the composite cathode and on particle-size engineering [96] (insufficient evidence at practical loading). G4 is challenged by the moisture sensitivity of sulfides during processing [3] and by sulfide-specific and cathode-oxygen-driven runaway pathways [53,55] (insufficient full-cell abuse data). The lowest outcomes therefore occur at G3 and G4, with G2 conditional; the binding constraints lie in contact evolution, composite transport at practical loading and processing, rather than in electrolyte conductivity, and AI effort would be most useful for contact evolution and processing windows.

Worked example 2: garnet | lithium metal. G1 is close to thermodynamic stability [22] (pass); G2 depends on a wetting interlayer [12] and on the critical stripping current (conditional pass); G3 is compromised by electronic leakage [72,73] (conditional pass or fail, depending on microstructure); and G4 is limited by thin-separator processing [11] and by the runaway pathway involving molten lithium [51] (insufficient evidence). Here the binding constraints are G2 and G3, the gates at which AI evidence is weakest.

Table 17
Unresolved challenges and priorities for the roadmap in Fig. 15, with the sections in which each limitation is identified.

Challenge	Why it matters	Current evidence	Required advance	Horizon	AI role (level)	Linked section
Interfacial resistance at practical loading	Dominates impedance (Gap 1)	Scattered; conditions unreported	Standardised measurement + MIDR datasets	Near	Learnable once data exist (L4 → L2)	9.1, 11
Passivation vs reactivity prediction	Controls interphase growth	AIMD-based classifiers	Experimental validation sets	Near	L2 → L1	6.2, 11
Contact evolution under cycling	Capacity fade in composites	Mechanistic studies	Operando imaging + mechanics datasets	Medium	L3	6.5, 8.3
Li-metal stripping/plating limits	Power and safety	Mechanisms established	Pressure–microstructure maps	Medium	L4 → L3	5.2, 6.6
Thin, large-area separators	Energy density; cost	Processing reviews	Defect-free scalable processing	Medium	BO for processing (L1 for bulk)	7
Reproducibility	Trust; data quality	Round robins	Reference materials and protocols	Near	Prerequisite for all AI	8.6, 12
Cell-level safety	Justifies SSBs	Scenario and calorimetry studies	Abuse tests of multilayer cells	Medium	L3 (surrogate thermal models)	3, 14
Universal-potential reliability at interfaces	Screening credibility	Softening documented	Interface-specific training data	Near–medium	L2	10.2, 11
Co-design of full cells	Avoids sequential sub-optimisation	Conceptual	Multi-objective closed loops with cell tests	Long	L3 → L1	13, 14
Polymer RT transport and transference	Limits room-temperature operation	Trade-offs documented	Decoupled transport and mechanics; method-consistent t_+	Medium	L2 (polymer σ models)	4.4
Transfer to sodium systems	Cost and resource security	Sulfide and polymer Na SEs	Na-specific gate evidence	Medium–long	L3	4.6

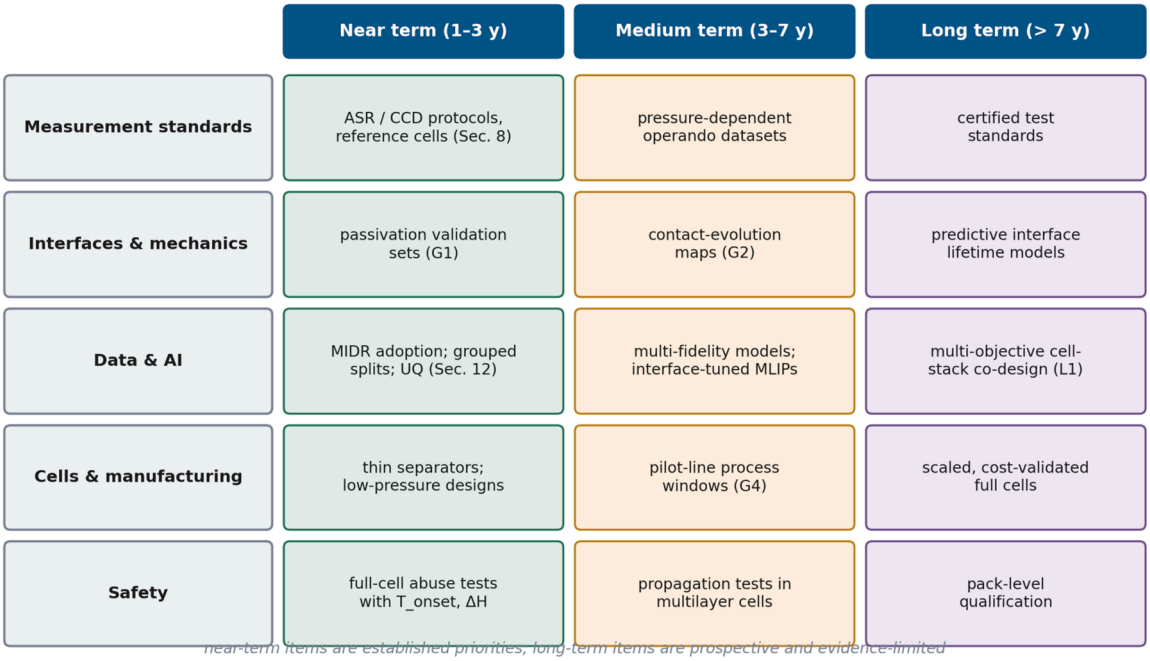


Fig. 15. Research roadmap. Priorities in five lanes (measurement standards, interfaces and mechanics, data and AI, cells and manufacturing, safety) over near-, medium- and long-term horizons. Near-term items are established priorities linked to limitations identified in Sections 8–14; long-term items are prospective. Based on Tables 13, 15–17 and Section 14.

The framework also exposes cross-gate conflicts that sequential design misses. Thicker coatings improve G1 but add resistance in G3; halide catholytes resolve G1 at the cathode but introduce a halide|sulfide junction that must itself pass G1 and G2; and higher stack pressure helps G2 for stripping but can promote filament propagation and adds system cost in G4 [27,29,60].

15. Unresolved contradictions, practical barriers and future perspectives

15.1. Contradictions that should be resolved rather than averaged

In our assessment, seven contradictions in the literature are more instructive than any consensus. (i) Space charge: first-principles and NMR evidence that it matters [97,99] versus modelling indicating that it is negligible except under strong depletion [98]. (ii) Stack pressure: beneficial for stripping but harmful for filament propagation [27,60]. (iii) Stability windows: narrow thermodynamic windows [14] versus wider practical windows and widespread passivation [26,59]. (iv) Mechanical criteria: modulus-based suppression criteria [61,107] versus penetration of stiff ceramics through defects and electronic pathways [72,100]. (v) Safety: non-flammable materials [3] versus cell-level runaway pathways [51,57]. (vi) AI discovery: millions of predicted materials versus critiques of novelty and utility [36,37]. (vii) Systematic softening and activation-energy bias of universal potentials [38,62] versus claims of readiness for solid ion conductors [120]. Each contradiction is resolved by stating conditions (depletion, pressure window, passivation chemistry, flaw population, cell energy, validation criteria, fine-tuning), thereby supporting the metadata standard in Box 1.

15.2. Practical barriers

Cell-level benchmarks are energy density and power at practical separator thickness and areal loading, cycle life under a stack pressure that a pack can provide, operating-temperature range and cost [28,29,104]. Laboratory reports rarely address manufacturing requirements such as large-area thin separators [11], dry-room or inert processing for sulfides, lithium handling and scalable coating processes [126]. Safety must be demonstrated by full-cell abuse tests rather than inferred from electrolyte flammability [57]. New materials should be reported with the cell-level variables of Box 1 and, where feasible, compared with a common reference cell [28].

15.3. Future research directions linked to the identified limitations

The directions below follow from specific limitations identified in this review (Table 17, Fig. 15). We distinguish established priorities, supported by documented problems, from prospective possibilities that remain speculative.

Established priorities. (1) **Standardised interface-testing protocols.** The inter-laboratory spreads in conductivity and cell performance (Sections 4.2 and 6.7) [30,31] show that common protocols for ASR, CCD and cycling, including pressure, temperature, step size and replicate number, are prerequisites for comparison and for any data-driven model. (2) **Pressure-dependent interface characterisation.** Because pressure affects stripping, filament propagation, apparent conductivity and thermal behaviour in different directions [27,60,69,102,103], interface metrics should be reported as functions of pressure, ideally with in situ pressure monitoring. (3) **Quantitative failure criteria.** The gate criteria of Table 15 require prospective testing: does a design that passes all four gates on laboratory evidence also pass them in multilayer pouch cells? (4) **Data and metadata standards.** Adoption of an interface record such as the MIDR (Box 1), including negative results, would address the data asymmetry of Section 12. (5) **Uncertainty-aware screening and transferable models.** Fine-tuning of universal potentials on reactive interface configurations [38], grouped data splits, calibrated uncertainty and prospective tests [45,46] address the method bias and leakage identified in Sections 10–12. (6) **Integration of theory, synthesis and electrochemical validation.** Closed loops have been demonstrated for bulk synthesis [34,89]; extending them to interface-processing variables (coating thickness, densification, pressure windows) is the next step (Section 13). (7) **Interface-sensitive operando measurements** linked to standard cell tests (Section 8.5). (8) **Scale-up, safety and techno-economics.** Thin separators,

low-pressure operation, dry-room requirements and full-cell abuse data with the metrics of Table 16 determine practical viability [11,29,57,104,126].

Prospective possibilities. Multi-objective AI co-design of complete cell stacks evaluated on validated cell-level metrics, predictive models of interface lifetime, and transfer of the framework to sodium and other post-lithium chemistries once their own gate evidence exists (Section 4.6) are plausible but not yet supported by demonstrations; their realisation depends on the established priorities above.

Fig. 15 arranges these directions by time horizon. In the near term (1–3 years), the most useful investments are infrastructural: adoption of the MIDR, interface-specific training data for fine-tuning universal potentials, and experimental validation sets for passivation classifiers. In the medium term (3–7 years), closed-loop optimisation should be extended from bulk synthesis and computer simulation to interface processing (coating thickness, densification profiles, pressure windows), operando datasets should be connected to the evolving contact microstructure, and multi-fidelity models should combine computational and experimental labels. In the long term (>7 years), the objective is multi-objective co-design in which AI proposes entire cell stacks (electrolyte, electrodes, interlayers and processing) that are evaluated on validated cell-level metrics rather than on the accuracy of property predictions.

16. Conclusions

Ionic conductivity, long regarded as the most pressing problem for solid-state batteries, is no longer the main obstacle for the leading electrolyte families reviewed here. The limiting processes occur at interfaces, where chemistry, electrochemistry, mechanics and transport are coupled and where thermodynamic stability is neither necessary (passivating interphases) nor sufficient (contact loss and electronic leakage). Our resistance analysis indicates that, once separators are thin and exceed ~1 mS cm^{-1}, interfacial and composite-electrode resistances dominate ohmic loss, and that measured interfacial resistances for a single materials pair can differ by more than three orders of magnitude depending on processing. The safety benefit is real but conditional: it depends on the stored energy of the complete cell, on interphase chemistry and on electrode crosstalk, and it must be demonstrated by full-cell abuse testing rather than assumed.

Polymer-based electrolytes form a distinct family whose solid, gel/quasi-solid and composite members differ in transport mechanism, safety and stability and should not be treated as interchangeable; their central trade-off is between ionic mobility and mechanical or electrochemical robustness. Reliable conclusions about any interface require complementary techniques reported under stated conditions, because impedance, critical-current and cycling data depend strongly on pressure, temperature, cell configuration and analysis choices.

AI is already useful, but its validated successes are concentrated where data are abundant and experiments are fast: bulk stability and conductivity screening within known chemistries, and low-dimensional synthesis optimisation with direct measurement. Graded on two explicit scales, interface prediction remains largely computational (Level 2, validation-scale grade D), based on tens of simulations and bounded by an experimental noise floor of 35–50% relative standard deviation in conductivity. Prominent claims of AI discovery are contested, and systematic biases in universal potentials affect transport predictions.

In our view, three changes could advance the field faster than any single material or algorithm: training labels that describe cell-level failure modes rather than bulk properties; reporting standards, such as the proposed Minimum Interface Data Record, that make interface data reusable; and co-design workflows in which electrolyte, electrode, interface and processing must pass the same operationally defined validity gates. The proposed gates and screening targets are design tools that still require prospective testing. Under these conditions, AI could progress from predicting materials to designing functional interfaces.

Funding

This research did not receive any specific grant from funding agencies in the public, commercial, or not-for-profit sectors.

Declaration of generative AI and AI-assisted technologies in the manuscript preparation process

During the preparation of the revised manuscript, the authors used ChatGPT (OpenAI) for limited assistance with English-language editing and improving the clarity of selected passages. The original scientific content, interpretation, and manuscript writing were produced by the authors. The authors reviewed and approved all revisions and take full responsibility for the accuracy, originality, and integrity of the manuscript.

CRediT authorship contribution statement

Mohammed Tihtih: Writing – review & editing, Writing – original draft, Visualization, Validation, Methodology, Investigation, Formal analysis, Data curation. **Abdellah Ben yahia:** Formal analysis, Data curation. **Redouane En-nadir:** Investigation, Data curation. **M. A. Basyooni-M. Kabatas:** Funding acquisition. **István Kocserha:** Supervision.

Declaration of competing interest

The authors declare that they have no known competing financial interests or personal relationships that could have appeared to influence the work reported in this manuscript.

Acknowledgements

The authors acknowledge the Institute of Energy, Ceramics, and Polymer Technology, University of Miskolc, for institutional support and access to research resources.

Data availability

This article is a review and reports no new experimental data. All numerical values compiled in the text, tables and figures are taken from the cited sources, with measurement conditions stated where available; derived values are identified as such and can be reproduced from Eqs. (1)–(3) and the inputs listed in Table 10.

References

[1] J. Janek, W.G. Zeier, A solid future for battery development, Nat. Energy 1 (2016) 16141, https://doi.org/10.1038/nenergy.2016.141.
[2] A. Manthiram, X. Yu, S. Wang, Lithium battery chemistries enabled by solid-state electrolytes, Nat. Rev. Mater. 2 (2017) 16103, https://doi.org/10.1038/natrevmats.2016.103.
[3] Q. Zhao, S. Stalin, C.-Z. Zhao, L.A. Archer, Designing solid-state electrolytes for safe, energy-dense batteries, Nat. Rev. Mater. 5 (2020) 229–252, https://doi.org/10.1038/s41578-019-0165-5.
[4] X. Feng, M. Ouyang, X. Liu, L. Lu, Y. Xia, X. He, Thermal runaway mechanism of lithium ion battery for electric vehicles: a review, Energy Storage Mater. 10 (2018) 246–267.
[5] N. Kamaya, K. Homma, Y. Yamakawa, M. Hirayama, R. Kanno, M. Yonemura, T. Kamiyama, Y. Kato, S. Hama, K. Kawamoto, A. Mitsui, A lithium superionic conductor, Nat. Mater. 10 (2011) 682–686, https://doi.org/10.1038/nmat3066.
[6] Y. Seino, T. Ota, K. Takada, A. Hayashi, M. Tatsumisago, A sulphide lithium super ion conductor is superior to liquid ion conductors for use in rechargeable batteries, Energy Environ. Sci. 7 (2014) 627–631, https://doi.org/10.1039/C3EE41655K.
[7] Y. Kato, S. Hori, T. Saito, K. Suzuki, M. Hirayama, A. Mitsui, M. Yonemura, H. Iba, R. Kanno, High-power all-solid-state batteries using sulfide superionic conductors, Nat. Energy 1 (2016) 16030, https://doi.org/10.1038/nenergy.2016.30.
[8] R. Murugan, V. Thangadurai, W. Weppner, Fast lithium ion conduction in garnet-type Li7La3Zr2O12, Angew. Chem. Int. Ed. 46 (2007) 7778–7781.

[9] T. Asano, A. Sakai, S. Ouchi, M. Sakaida, A. Miyazaki, S. Hasegawa, Solid halide electrolytes with high lithium-ion conductivity for application in 4 V class bulk-type all-solid-state batteries, Adv. Mater. 30 (2018) 1803075, https://doi.org/10.1002/adma.201803075.

[10] Y. Tanaka, K. Ueno, K. Mizuno, K. Takeuchi, T. Asano, A. Sakai, New oxyhalide solid electrolytes with high lithium ionic conductivity >10 mS cm-1 for all-solid-state batteries, Angew. Chem. Int. Ed. 62 (2023) e202217581, https://doi.org/10.1002/anie.202217581.

[11] M. Balaish, J.C. Gonzalez-Rosillo, K.J. Kim, Y. Zhu, Z.D. Hood, J.L.M. Rupp, Processing thin but robust electrolytes for solid-state batteries, Nat. Energy 6 (2021) 227–239, https://doi.org/10.1038/s41560-020-00759-5.

[12] X. Han, Y. Gong, K. Fu, X. He, G.T. Hitz, J. Dai, A. Pearse, B. Liu, H. Wang, G. Rubloff, Y. Mo, V. Thangadurai, E.D. Wachsman, L. Hu, Negating interfacial impedance in garnet-based solid-state Li metal batteries, Nat. Mater. 16 (2017) 572–579, https://doi.org/10.1038/nmat4821.

[13] H.-J. Deiseroth, et al., Li6PS5X: a class of crystalline Li-rich solids with an unusually high Li+ mobility, Angew. Chem. Int. Ed. 47 (2008) 755–758.

[14] W.D. Richards, L.J. Miara, Y. Wang, J.C. Kim, G. Ceder, Interface stability in solid-state batteries, Chem. Mater. 28 (2016) 266–273.

[15] F. Han, Y. Zhu, X. He, Y. Mo, C. Wang, Electrochemical stability of Li10GeP2S12 and Li7La3Zr2O12 solid electrolytes, Adv. Energy Mater. 6 (2016) 1501590, https://doi.org/10.1002/aenm.201501590.

[16] H. Kwak, S. Wang, J. Park, Y. Liu, K.T. Kim, Y. Choi, Y. Mo, Y.S. Jung, Emerging halide superionic conductors for all-solid-state batteries: design, synthesis, and practical applications, ACS Energy Lett. 7 (2022) 1776–1805.

[17] F. Croce, G.B. Appetecchi, L. Persi, B. Scrosati, Nanocomposite polymer electrolytes for lithium batteries, Nature 394 (1998) 456–458, https://doi.org/10.1038/28818.

[18] J. Mindemark, M.J. Lacey, T. Bowden, D. Brandell, Beyond PEO, alternative host materials for Li*-conducting solid polymer electrolytes, Prog. Polym. Sci. 81 (2018) 114–143.

[19] W. Liu, N. Liu, J. Sun, P.-C. Hsu, Y. Li, H.-W. Lee, Y. Cui, Ionic conductivity enhancement of polymer electrolytes with ceramic nanowire fillers, Nano Lett. 15 (2015) 2740–2745, https://doi.org/10.1021/acs.nanolett.5b00600.

[20] A. Hayashi, K. Noi, A. Sakuda, M. Tatsumisago, Superionic glass-ceramic electrolytes for room-temperature rechargeable sodium batteries, Nat. Commun. 3 (2012) 856, https://doi.org/10.1038/ncomms1843.

[21] V.S. Kala, N. Singh, C.B. Soni, Sungjemmenla, M. Chandra, Tushar, Y. Yamauchi, M. Han, V. Kumar, When solid polymers meet Na-ions: unraveling solvation dynamics and molecular design principles for next-generation high-energy sodium metal batteries, J. Mater. Chem. A 14 (2026) 4894–4932, https://doi.org/10.1039/D5TA07060K.

[22] Y. Xiao, Y. Wang, S.-H. Bo, J.C. Kim, L.J. Miara, G. Ceder, Understanding interface stability in solid-state batteries, Nat. Rev. Mater. 5 (2020) 105–126, https://doi.org/10.1038/s41578-019-0157-5.

[23] A. Banerjee, X. Wang, C. Fang, E.A. Wu, Y.S. Meng, Interfaces and interphases in all-solid-state batteries with inorganic solid electrolytes, Chem. Rev. 120 (2020) 6878–6933.

[24] S. Kalnaus, N.J. Dudney, A.S. Westover, E. Herbert, S. Hackney, Solid-state batteries: the critical role of mechanics, Science 381 (2023) eabg5998, https://doi.org/10.1126/science.abg5998.

[25] R. Koerver, I. Aygün, T. Leichtwei, C. Dietrich, W. Zhang, J.O. Binder, P. Hartmann, W.G. Zeier, J. Janek, Capacity fade in solid-state batteries: interphase formation and chemomechanical processes in nickel-rich layered oxide cathodes and lithium thiophosphate solid electrolytes, Chem. Mater. 29 (2017) 5574–5582, https://doi.org/10.1021/acs.chemmater.7b00931.

[26] T.K. Schwietert, V.A. Arszelewska, C. Wang, C. Yu, A. Vasileiadis, N.J.J. de Klerk, J. Hageman, T. Hupfer, I. Kerkamm, Y. Xu, E. van der Maas, E.M. Kelder, S. Ganapathy, M. Wagemaker, Clarifying the relationship between redox activity and electrochemical stability in solid electrolytes, Nat. Mater. 19 (2020) 428–435, https://doi.org/10.1038/s41563-019-0576-0.

[27] J. Kasemchainan, S. Zekoll, D. Spencer Jolly, Z. Ning, G.O. Hartley, J. Marrow, P. G. Bruce, Critical stripping current leads to dendrite formation on plating in lithium anode solid electrolyte cells, Nat. Mater. 18 (2019) 1105–1111, https://doi.org/10.1038/s41563-019-0438-9.

[28] S. Randau, D.A. Weber, O. Kötz, R. Koerver, P. Braun, A. Weber, E. Ivers-Tiffée, T. Adermann, J. Kulisch, W.G. Zeier, F.H. Richter, J. Janek, Benchmarking the performance of all-solid-state lithium batteries, Nat. Energy 5 (2020) 259–270, https://doi.org/10.1038/s41560-020-0565-1.

[29] J. Janek, W.G. Zeier, Challenges in speeding up solid-state battery development, Nat. Energy 8 (2023) 230–240, https://doi.org/10.1038/s41560-023-01208-9.

[30] S. Puls, E. Nazmutdinova, F. Kalyk, W.G. Zeier, N.M. Vargas-Barbosa, Benchmarking the reproducibility of all-solid-state battery cell performance, Nat. Energy 9 (2024) 1310–1320, https://doi.org/10.1038/s41560-024-01634-3.

[31] S. Ohno, T. Bernges, J. Buchheim, N.M. Vargas-Barbosa, W.G. Zeier, How certain are the reported ionic conductivities of thiophosphate-based solid electrolytes? An interlaboratory study, ACS Energy Lett. 5 (2020) 910–915, https://doi.org/10.1021/acsenergylett.9b02764.

[32] A. Merchant, S. Batzner, S.S. Schoenholz, M. Aykol, G. Cheon, E.D. Cubuk, Scaling deep learning for materials discovery, Nature 624 (2023) 80–85, https://doi.org/10.1038/s41586-023-06735-9.

[33] C. Chen, D.T. Nguyen, S.J. Lee, N.A. Baker, A.S. Karakoti, L. Lauw, C. Owen, K. T. Mueller, B.A. Bilodeau, V. Murugesan, M. Troyer, Accelerating computational materials discovery with machine learning and cloud high-performance computing: from large-scale screening to experimental validation, J. Am. Chem. Soc. 146 (2024) 20009–20018, https://doi.org/10.1021/jacs.4c03849.

[34] [authors/title: complete from DOI record], Bayesian optimization of the solid-state synthesis of tetragonal Li7SiPS8 (publisher version deposited in KITopen), KITopen repository (publisher version) (2026), https://doi.org/10.5445/IR/1000193723.

[35] N.J. Szymanski, B. Rendy, Y. Fei, et al., An autonomous laboratory for the accelerated synthesis of novel materials, Nature 624 (2023) 86–91.

[36] J. Leeman, Y. Liu, J. Stiles, S.B. Lee, P. Bhatt, L.M. Schoop, R.G. Palgrave, Challenges in high-throughput inorganic materials prediction and autonomous synthesis, PRX Energy 3 (2024) 011002, https://doi.org/10.1103/PRXEnergy.3.011002.

[37] A.K. Cheetham, R. Seshadri, Artificial intelligence driving materials discovery? Perspective on the article: scaling deep learning for materials discovery, Chem. Mater. 36 (2024) 3490–3495, https://doi.org/10.1021/acs.chemmater.4c00643.

[38] B. Deng, Y. Choi, P. Zhong, J. Riebesell, S. Anand, Z. Li, K. Jun, K.A. Persson, G. Ceder, Systematic softening in universal machine learning interatomic potentials, npj Comput. Mater. 11 (2025) 9, https://doi.org/10.1038/s41524-024-01500-6.

[39] T. Lombardo, M. Duquesnoy, H. El-Bouysidy, A.A. Franco, Artificial intelligence applied to battery research: hype or reality? Chem. Rev. 122 (2022) 10899–10969, https://doi.org/10.1021/acs.chemrev.1c00108.

[40] Z. Zheng, J. Zhou, Y. Zhu, Computational approach inspired advancements of solid-state electrolytes for lithium secondary batteries: from first-principles to machine learning, Chem. Soc. Rev. 53 (2024) 3134–3166, https://doi.org/10.1039/D3CS00572K.

[41] A.C.C. Dutra, B.A. Goldmann, M.S. Islam, J.A. Dawson, Understanding solid-state battery electrolytes using atomistic modelling and machine learning, Nat. Rev. Mater. 10 (2025) 566–583. https://researchportal.bath.ac.uk/en/publications/understanding-solid-state-battery-electrolytes-using-atomistic-mo/.

[42] Z. Wang, W.G. Zeier, F. You, Toward AI ecosystems for electrolyte and interface engineering in solid-state batteries, Sci. Adv. 11 (2025) eaea0638, https://doi.org/10.1126/sciadv.aea0638.

[43] S. Wang, J. Liu, X. Song, H. Xu, Y. Gu, J. Fan, B. Sun, L. Yu, Artificial intelligence empowers solid-state batteries for material screening and performance evaluation, Nano-Micro Lett. 17 (2025) 287, https://doi.org/10.1007/s40820-025-01797-y.

[44] Q. Hu, K. Chen, J. Li, T. Zhao, F. Liang, D. Xue, Artificial intelligence-driven development in rechargeable battery materials: progress, challenges, and future perspectives, Adv. Funct. Mater. 36 (2026) 2507474, https://doi.org/10.1002/adfm.202507474.

[45] N. Artrith, K.T. Butler, F.-X. Coudert, S. Han, O. Isayev, A. Jain, A. Walsh, Best practices in machine learning for chemistry, Nat. Chem. 13 (2021) 505–508, https://doi.org/10.1038/s41557-021-00716-z.

[46] A. Bender, et al., Evaluation guidelines for machine learning tools in the chemical sciences, Nat. Rev. Chem. 6 (2022) 428–442, https://doi.org/10.1038/s41570-022-00391-9.

[47] G.H. Guyatt, A.D. Oxman, G.E. Vist, R. Kunz, Y. Falck-Ytter, P. Alonso-Coello, H. J. Schünemann, GRADE: an emerging consensus on rating quality of evidence and strength of recommendations, BMJ 336 (2008) 924–926, https://doi.org/10.1136/bmj.39489.470347.AD.

[48] T. Famprikis, P. Canepa, J.A. Dawson, M.S. Islam, C. Masquelier, Fundamentals of inorganic solid-state electrolytes for batteries, Nat. Mater. 18 (2019) 1278–1291, https://doi.org/10.1038/s41563-019-0431-3.

[49] J.C. Bachman, et al., Inorganic solid-state electrolytes for lithium batteries: mechanisms and properties governing ion conduction, Chem. Rev. 116 (2016) 140–162.

[50] [authors: complete from DOI record], AI agents for solid electrolytes: opportunities, challenges, and future directions, AI Agent 1 (2025) 10, https://doi.org/10.20517/aiagent.2025.10.

[51] R. Chen, A.M. Nolan, J. Lu, J. Wang, X. Yu, Y. Mo, L. Chen, X. Huang, H. Li, The thermal stability of lithium solid electrolytes with metallic lithium, Joule 4 (2020) 812–821, https://doi.org/10.1016/j.joule.2020.03.012.

[52] T. Inoue, K. Mukai, Are all-solid-state lithium-ion batteries really safe? Verification by differential scanning calorimetry with an all-inclusive microcell, ACS Appl. Mater. Interfaces 9 (2017) 1507–1515.

[53] X. Rui, D. Ren, X. Liu, X. Wang, K. Wang, Y. Lu, L. Li, P. Wang, G. Zhu, Y. Mao, X. Feng, L. Lu, H. Wang, M. Ouyang, Distinct thermal runaway mechanisms of sulfide-based all-solid-state batteries, Energy Environ. Sci. 16 (2023) 3552–3563, https://doi.org/10.1039/D3EE00084B.

[54] Y. Wu, J. Xu, P. Lu, et al., Thermal stability of the sulfide solid electrolyte with lithium metal, Adv. Energy Mater. 13 (2023) 2301336, https://doi.org/10.1002/aenm.202301336.

[55] S.-J. Yang, J.-K. Hu, F.-N. Jiang, et al., Oxygen-induced thermal runaway mechanisms of ah-level solid-state lithium metal pouch cells, eTransportation 18 (2023) 100279, https://doi.org/10.1016/j.etran.2023.100279.

[56] B.S. Vishnugopi, M.T. Hasan, H. Zhou, et al., Interphases and electrode crosstalk dictate the thermal stability of solid-state batteries, ACS Energy Lett. 8 (2023) 398–407, https://doi.org/10.1021/acsenergylett.2c02443.

[57] A.M. Bates, Y. Preger, L. Torres-Castro, K.L. Harrison, S.J. Harris, J. Hewson, Are solid-state batteries safer than lithium-ion batteries? Joule 6 (2022) 742–755, https://doi.org/10.1016/j.joule.2022.02.007.

[58] Y. Li, S. Song, H. Kim, et al., A lithium superionic conductor for millimeter-thick battery electrode, Science 381 (2023) 50–53, https://doi.org/10.1126/science.add7138.

[59] E.G. Lomeli, B. Ransom, A. Ramdas, D. Jost, B. Moritz, A.D. Sendek, E.J. Reed, T. P. Devereaux, Predicting reactivity and passivation of solid-state battery

interfaces, ACS Appl. Mater. Interfaces 16 (2024) 51584–51594, https://doi.org/10.1021/acsami.4c06095.
[60] Z. Ning, G. Li, D.L.R. Melvin, C.W. Monroe, P.G. Bruce, Dendrite initiation and propagation in lithium metal solid-state batteries, Nature 618 (2023) 287–293, https://doi.org/10.1038/s41586-023-05970-4.
[61] C. Monroe, J. Newman, The impact of elastic deformation on deposition kinetics at lithium/polymer interfaces, J. Electrochem. Soc. 152 (2005), https://doi.org/10.1149/1.1850854.
[62] X. Guo, Z. Wang, J. Yang, X. Gong, Machine-learning assisted high-throughput discovery of solid-state electrolytes for Li-ion batteries, J. Mater. Chem. A 12 (2024) 10124–10136, https://doi.org/10.1039/D4TA00721B.
[63] Y. Xiao, L.J. Miara, Y. Wang, G. Ceder, Computational screening of cathode coatings for solid-state batteries, Joule 3 (2019) 1252–1275, https://doi.org/10.1016/j.joule.2019.02.006.
[64] Y.-Q. Zhang, Y. Tian, Y. Xiao, L.J. Miara, Y. Aihara, T. Tsujimura, T. Shi, M. C. Scott, G. Ceder, Direct visualization of the interfacial degradation of cathode coatings in solid state batteries: a combined experimental and computational study, Adv. Energy Mater. 10 (2020) 1903778, https://doi.org/10.1002/aenm.201903778.
[65] L. Zhou, et al., High areal capacity, long cycle life 4 V ceramic all-solid-state Li-ion batteries enabled by chloride solid electrolytes, Nat. Energy 7 (2022) 83–93, https://doi.org/10.1038/s41560-021-00952-0.
[66] Y.-G. Lee, et al., High-energy long-cycling all-solid-state lithium metal batteries enabled by silver-carbon composite anodes, Nat. Energy 5 (2020) 299–308, https://doi.org/10.1038/s41560-020-0575-z.
[67] D.H.S. Tan, Y.-T. Chen, H. Yang, et al., Chen, Z.; Meng, Y. S. Carbon-free high-loading silicon anodes enabled by sulfide solid electrolytes, Science 373 (2021) 1494–1499, https://doi.org/10.1126/science.abg7217.
[68] N. Johnson, P. Albertus, Modeling thermal behavior and safety of large format all-solid-state lithium metal batteries under thermal ramp and short circuit conditions, J. Electrochem. Soc. (2022) 169.
[69] Y. Wu, W. Zhang, X. Rui, D. Ren, C. Xu, X. Liu, X. Feng, Z. Ma, L. Lu, M. Ouyang, Thermal runaway mechanism of composite cathodes for all-solid-state batteries, Adv. Energy Mater. 15 (2025) 2405183, https://doi.org/10.1002/aenm.202405183.
[70] Y. Li, X. Chen, A. Dolocan, Z. Cui, S. Xin, L. Xue, H. Xu, K. Park, J.B. Goodenough, Garnet electrolyte with an ultralow interfacial resistance for Li-metal batteries, J. Am. Chem. Soc. 140 (2018) 6448–6455. https://scholars.ln.edu.hk/en/publications/garnet-electrolyte-with-an-ultralow-interfacial-resistance-for-li/.
[71] E.J. Cheng, A. Sharafi, J. Sakamoto, Intergranular Li metal propagation through polycrystalline Li6.25Al0.25La3Zr2O12 ceramic electrolyte, Electrochim. Acta 223 (2017) 85–91.
[72] F. Han, A.S. Westover, J. Yue, X. Fan, F. Wang, M. Chi, D.N. Leonard, N. J. Dudney, H. Wang, C. Wang, High electronic conductivity as the origin of lithium dendrite formation within solid electrolytes, Nat. Energy 4 (2019) 187–196, https://doi.org/10.1038/s41560-018-0312-z.
[73] X. Liu, R. Garcia-Mendez, A.R. Lupini, et al., Local electronic structure variation resulting in Li 'filament' formation within solid electrolytes, Nat. Mater. 20 (2021) 1485–1490.
[74] R. Pfenninger, M. Struzik, I. Garbayo, E. Stilp, J.L.M Rupp, A low ride on processing temperature for fast lithium conduction in garnet solid-state battery films, Nat. Energy 4 (2019) 475–483.
[75] Z.D. Hood, Y. Zhu, L.J. Miara, W.S. Chang, P. Simons, J.L.M. Rupp, A sinter-free future for solid-state battery designs, Energy Environ. Sci. 15 (2022) 2927–2936.
[76] K.J. Kim, J.L.M Rupp, All ceramic cathode composite design and manufacturing towards low interfacial resistance for garnet-based solid-state lithium batteries, Energy Environ. Sci. 13 (2020) 4930–4945.
[77] P. Adeli, et al., Boosting solid-state diffusivity and conductivity in lithium superionic argyrodites by halide substitution, Angew. Chem. Int. Ed. 58 (2019) 8681–8686.
[78] S. Wenzel, et al., Direct observation of the interfacial instability of the fast ionic conductor $Li_{10}GeP_2S_{12}$ at the lithium metal anode, Chem. Mater. 28 (2016) 2400–2407.
[79] A.-Y. Kim, F. Strauss, T. Bartsch, J.H. Teo, J. Janek, T. Brezesinski, Effect of surface carbonates on the cyclability of LiNbO3-coated NCM622 in all-solid-state batteries with lithium thiophosphate electrolytes, Sci. Rep. 11 (2021) 11, https://doi.org/10.1038/s41598-021-84799-1.
[80] X. Li, J. Liang, J. Luo, et al., Air-stable Li3InCl6 electrolyte with high voltage compatibility for all-solid-state batteries, Energy Environ. Sci. 12 (2019) 2665–2671.
[81] C. Wang, J. Liang, J.T. Kim, X. Sun, Prospects of halide-based all-solid-state batteries: from material design to practical application, Sci. Adv. 8 (2022) eadc9516, https://doi.org/10.1126/sciadv.adc9516.
[82] B. Singh, Y. Wang, J. Liu, J.D. Bazak, A. Shyamsunder, L.F. Nazar, Critical role of framework flexibility and disorder in driving high ionic conductivity in LiNbOCl4, J. Am. Chem. Soc. 146 (2024) 17158–17169. https://impact.ornl.gov/en/publications/critical-role-of-framework-flexibility-and-disorder-in-driving-hi/.
[83] D. Lin, W. Liu, Y. Liu, H.R. Lee, P.-C. Hsu, K. Liu, Y. Cui, High ionic conductivity of composite solid polymer electrolyte via in situ synthesis of monodispersed SiO_2 nanospheres in poly(ethylene oxide), Nano Lett. 16 (2016) 459–465, https://doi.org/10.1021/acs.nanolett.5b04117.
[84] L. Porcarelli, M.A. Aboudzadeh, L. Rubatat, J.R. Nair, A.S. Shaplov, C. Gerbaldi, D. Mecerreyes, Single-ion triblock copolymer electrolytes based on poly(ethylene oxide) and methacrylic sulfonamide blocks for lithium metal batteries, J. Power Sources 364 (2017) 191–199, https://doi.org/10.1016/j.jpowsour.2017.08.023.
[85] Q. Zhao, X. Liu, S. Stalin, K. Khan, L.A. Archer, Solid-state polymer electrolytes with in-built fast interfacial transport for secondary lithium batteries, Nat. Energy 4 (2019) 365–373, https://doi.org/10.1038/s41560-019-0349-7.
[86] J. Evans, C.A. Vincent, P.G. Bruce, Electrochemical measurement of transference numbers in polymer electrolytes, Polymer 28 (1987) 2324–2328, https://doi.org/10.1016/0032-3861(87)90394-6.
[87] P.G. Bruce, M.T. Hardgrave, C.A. Vincent, The determination of transference numbers in solid polymer electrolytes using the Hittorf method, Solid State Ionics 53-56 (1992) 1087–1094.
[88] G. Bradford, J. Lopez, J. Ruza, M.A. Stolberg, R. Osterude, J.A. Johnson, R. Gomez-Bombarelli, Y. Shao-Horn, Chemistry-informed machine learning for polymer electrolyte discovery, ACS Cent. Sci. 9 (2023) 206–216, https://doi.org/10.1021/acscentsci.2c01123.
[89] [authors: complete from ChemRxiv record], Autonomous discovery of polymer electrolyte formulations with warm-start batch Bayesian optimization, ChemRxiv (2025). https://chemrxiv.org/engage/chemrxiv/article-details/67e46e95fa469535b99df4ee [Preprint; not peer reviewed].
[90] R. Koerver, W. Zhang, L. de Biasi, S. Schweidler, A.O. Kondrakov, S. Kolling, T. Brezesinski, P. Hartmann, W.G. Zeier, J. Janek, Chemo-mechanical expansion of lithium electrode materials - on the route to mechanically optimized all-solid-state batteries, Energy Environ. Sci. 11 (2018) 2142–2158.
[91] H.-H. Ryu, B. Namkoong, J.-H. Kim, I. Belharouak, C.S. Yoon, Y.-K. Sun, Capacity fading mechanisms in Ni-rich single-crystal NCM cathodes, ACS Energy Lett. 6 (2021) 2726–2734.
[92] C.D. Fincher, C. Gilgenbach, C. Roach, et al., Electrochemical corrosion accompanies dendrite growth in solid electrolytes, Nature 652 (2026) 906–911.
[93] S. Cangaz, F. Hippauf, F.S. Reuter, et al., Enabling high-energy solid-state batteries with stable anode interphase by the use of columnar silicon anodes, Adv. Energy Mater. 10 (2020) 2001320, https://doi.org/10.1002/aenm.202001320.
[94] W. Yan, et al., Hard-carbon-stabilized Li-Si anodes for high-performance all-solid-state Li-ion batteries, Nat. Energy 8 (2023) 800–813.
[95] J.A. Lewis, K.A. Cavallaro, Y. Liu, M.T. McDowell, The promise of alloy anodes for solid-state batteries, Joule 6 (2022) 1418–1430.
[96] T. Shi, Q. Tu, Y. Tian, Y. Xiao, L.J. Miara, O. Kononova, G. Ceder, High active material loading in all-solid-state battery electrode via particle size optimization, Adv. Energy Mater. 10 (2020) 1902881, https://doi.org/10.1002/aenm.201902881.
[97] J. Haruyama, et al., Space-charge layer effect at interface between oxide cathode and sulfide electrolyte in all-solid-state lithium-ion battery, Chem. Mater. 26 (2014) 4248–4255.
[98] N.J.J. de Klerk, M. Wagemaker, Space-charge layers in all-solid-state batteries; important or negligible? ACS Appl. Energy Mater. 1 (2018) 5609–5618, https://doi.org/10.1021/acsaem.8b01141.
[99] Z. Cheng, M. Liu, S. Ganapathy, et al., Wagemaker, M. Revealing the impact of space-charge layers on the Li-ion transport in all-solid-state batteries, Joule 4 (2020) 1311–1323. https://research.tudelft.nl/en/publications/revealing-the-impact-of-space-charge-layers-on-the-li-ion-transpo.
[100] L. Porz, T. Swamy, B.W. Sheldon, et al., Mechanism of lithium metal penetration through inorganic solid electrolytes, Adv. Energy Mater. 7 (2017) 1701003, https://doi.org/10.1002/aenm.201701003.
[101] F. Flatscher, M. Philipp, S. Ganschow, H.M.R. Wilkening, D. Rettenwander, The natural critical current density limit for Li7La3Zr2O12 garnets, J. Mater. Chem. A 8 (2020) 15782–15788.
[102] J.-M. Doux, H. Nguyen, et al., Meng, Y. S. Stack pressure considerations for room-temperature all-solid-state lithium metal batteries, Adv. Energy Mater. 10 (2020) 1903253, https://doi.org/10.1002/aenm.201903253.
[103] J.-M. Doux, Y. Yang, D.H.S. Tan, H. Nguyen, E.A. Wu, et al., Pressure effects on sulfide electrolytes for all solid-state batteries, J. Mater. Chem. A 8 (2020) 5049–5055, https://doi.org/10.1039/C9TA12889A.
[104] P. Albertus, V. Anandan, C. Ban, et al., Challenges for and pathways toward Li-metal-based all-solid-state batteries, ACS Energy Lett. 6 (2021) 1399–1404.
[105] P. Vadhva, J. Hu, M.J. Johnson, R. Stocker, M. Braglia, D.J.L. Brett, A.J.E. Rettie, Electrochemical impedance spectroscopy for all-solid-state batteries: theory, methods and future outlook, ChemElectroChem 8 (2021) 1930–1947, https://doi.org/10.1002/celc.202100108.
[106] N. Ogihara, et al., Theoretical and experimental analysis of porous electrodes for lithium-ion batteries by electrochemical impedance spectroscopy using a symmetric cell, J. Electrochem. Soc. 159 (2012) A1034–A1039.
[107] Z. Ahmad, T. Xie, C. Maheshwari, J.C. Grossman, V. Viswanathan, Machine learning enabled computational screening of inorganic solid electrolytes for suppression of dendrite formation in lithium metal anodes, ACS Cent. Sci. 4 (2018) 996–1006, https://doi.org/10.1021/acscentsci.8b00229.
[108] Z. Ahmad, V. Viswanathan, Stability of electrodeposition at solid-solid interfaces and implications for metal anodes, Phys. Rev. Lett. 119 (2017) 056003, https://doi.org/10.1103/PhysRevLett.119.056003.
[109] R. Jalem, M. Nakayama, T. Kasuga, An efficient rule-based screening approach for discovering fast lithium ion conductors using density functional theory and artificial neural networks, J. Mater. Chem. A 2 (2014) 720–734, https://doi.org/10.1039/c3ta13235h.
[110] A.D. Sendek, Q. Yang, E.D. Cubuk, K.-A.N. Duerloo, Y. Cui, E.J. Reed, Holistic computational structure screening of >12 000 candidates for solid lithium-ion conductor materials, Energy Environ. Sci. 10 (2017) 306–320, https://doi.org/10.1039/C6EE02697D.
[111] A.D. Sendek, E.D. Cubuk, E.R. Antoniuk, G. Cheon, Y. Cui, E.J. Reed, Machine learning-assisted discovery of solid Li-ion conducting materials, Chem. Mater. 31 (2019) 342–352, https://doi.org/10.1021/acs.chemmater.8b03272.

[112] E.D. Cubuk, A.D. Sendek, E.J. Reed, Screening billions of candidates for solid lithium-ion conductors: a transfer learning approach for small data, J. Chem. Phys. 150 (2019) 214701, https://doi.org/10.1063/1.5093220.
[113] C.J. Hargreaves, M.W. Gaultois, L.M. Daniels, M.J. Rosseinsky, M.S. Dyer, A database of experimentally measured lithium solid electrolyte conductivities evaluated with machine learning, npj Comput. Mater. 9 (2023) 9, https://doi.org/10.1038/s41524-022-00951-z.
[114] C.J. Bartel, A. Trewartha, Q. Wang, A. Dunn, A. Jain, Ceder, G. A critical examination of compound stability predictions from machine-learned formation energies, npj Comput. Mater. 6 (2020) 6, https://doi.org/10.1038/s41524-020-00362-y.
[115] C. Chen, S.P. Ong, A universal graph deep learning interatomic potential for the periodic table, Nat. Comput. Sci. 2 (2022) 718–728.
[116] B. Deng, P. Zhong, K. Jun, J. Riebesell, K. Han, C.J. Bartel, G. Ceder, CHGNet as a pretrained universal neural network potential for charge-informed atomistic modelling, Nat. Mach. Intell. 5 (2023) 1031–1041.
[117] A. Vasylenko, J. Gamon, B.B. Duff, M.S. Dyer, M.J. Rosseinsky, Element selection for crystalline inorganic solid discovery guided by unsupervised machine learning of experimentally explored chemistry, Nat. Commun. 12 (2021) 5561, https://doi.org/10.1038/s41467-021-25343-7.
[118] P. Zhong, B. Deng, T. He, Z. Lun, G. Ceder, Deep learning of experimental electrochemistry for battery cathodes across diverse compositions, Joule 8 (2024) 1837–1854, https://doi.org/10.1016/j.joule.2024.03.010.
[119] C. Zeni, R. Pinsler, D. Zügner, et al., Xie, T. A generative model for inorganic materials design, Nature 639 (2025) 624–632.
[120] Du, H.; Hui, J.; Zhang, L.; Wang, H. Universal machine learning interatomic potentials are ready for solid ion conductors. *arXiv* 2025, 2502.09970. https://arxiv.org/abs/2502.09970 [Preprint; not peer reviewed].
[121] J. Gamon, et al., Computationally guided discovery of the sulfide Li3AlS3 in the Li-Al-S phase field: structure and lithium conductivity, Chem. Mater. 31 (2019) 9699–9714.
[122] A. Jain, S.P. Ong, G. Hautier, W. Chen, W.D. Richards, S. Dacek, S. Cholia, D. Gunter, D. Skinner, G. Ceder, K.A. Persson, Commentary: the Materials Project: a materials genome approach to accelerating materials innovation, APL Mater. 1 (2013) 011002.
[123] A. Dunn, Q. Wang, A. Ganose, D. Dopp, A. Jain, Benchmarking materials property prediction methods: the Matbench test set and Automatminer reference algorithm, npj Comput. Mater. 6 (2020) 138.
[124] Y. Wang, W.D. Richards, S.P. Ong, L.J. Miara, J.C. Kim, Y. Mo, G. Ceder, Design principles for solid-state lithium superionic conductors, Nat. Mater. 14 (2015) 1026–1031, https://doi.org/10.1038/nmat4369.
[125] K. Jun, et al., Lithium superionic conductors with corner-sharing frameworks, Nat. Mater. 21 (2022) 924–931, https://doi.org/10.1038/s41563-022-01222-4.
[126] J. Schnell, T. Günther, T. Knoche, et al., All-solid-state lithium-ion and lithium metal batteries - paving the way to large-scale production, J. Power Sources 382 (2018) 160–175.